Professur für
Thermofluiddynamik

MASTER

A Numerical Study on Premixed Laminar Flame Front Instabilities in Thermoacoustic Systems

Autor:
Abdel Karim Idris

Matrikel-No:
03649936

Betreuer:
Dipl.-Ing.Thomas Steinbacher, M. Sc.
Prof. Wolfgang Polifke, Ph. D.

December 15, 2016

Professur für Thermofluiddynamik
Prof. Wolfgang Polifke, Ph. D.

Erklärung

Hiermit versichere ich, die vorliegende Arbeit selbstständig verfasst zu haben. Ich habe keine anderen Quellen und Hilfsmittel als die angegebenen verwendet.

Ort, Datum	Abdel Karim Idris

Danksagung/Acknowledgement

This work is dedicated to M.Sc. Javier Achury, a former colleague at the "Professur für Thermofluiddynamik". The one whom I learned from a lot and who gave me the required prerequisites to start this work. I will be grateful to him for the rest of my life. May his body and soul rest in peace.

I would like to express my sincere gratitude to my master thesis supervisor Dipl.Ing. Thomas Steinbacher for the continuous support during the whole research period, for his patience, motivation, and immense knowledge. Not to mention the very useful research material supported by him. The door to Steinbacher's office was always open whenever I ran into a trouble or had a question about my research and he has always been steering me in the right direction.

I would also like to thank Prof. Polifke for supporting the master thesis's idea and finding the time to discuss it during my thesis defense and I am gratefully indebted for his very valuable comments on this thesis. Moreover, I would like to acknowledge M.Sc. Malte Merk for helping me to find the topic and the "Professur für Thermofluiddynamik" for giving me access to the computer laboratory and the required facilities during my work period.

Finally, I must express my very profound gratitude to my parents and my family for providing me with unfailing support and continuous encouragement throughout my years of study and through the process of researching and writing this thesis. This accomplishment would not have been possible without them. Thank you.

Kurzfassung/Abstract

In this project, our target is to numerically determine the flame transfer function of a conical flame, analyze the flame dynamics in response to the acoustic perturbations and try to find the connection between them. We start by introducing the thermo-acoustic systems as a simple model of several elements and briefly describe the flame transfer function. An analytical representation of the *FTF* is also represented. Regarding the flame dynamics we introduce the fundamental theories of laminar premixed flames. Moreover, we explain the flame instability and introduce two analytical models describing its growth rate. We then review some literature that include experimental determination of the Darrieus-Landau instability of V-Flames. We briefly describe our numerical setup before showing the results.

In the results, we start by introducing two excitation approaches, velocity and base temperature, and verify their similarity according to the flame heat release response. We then discuss the gain and phase of the *FTF* where the gain appears to reach a maximum value of higher than unity at around 80 Hz. We switch afterwards to looking at the flame front behavior for different harmonic frequencies and analyze the one with highest instability also at around 80 Hz. Results from the simulation are compared to theoretical relations from literature to verify the growth rates at different harmonics. We then try to find the reason for this instability using an impulsive excitation test, with an attempt to draw a conclusion from the observed unusual behavior of the *FTF* and the flame dynamics. The impulsive excitation produces a secondary wrinkle that lags the primary one with a time lag that is equivalent to 83 Hz. Further observations are then made with respect to the flame tip response which shows that the wrinkles are propagated with the convection velocity along the flame front. Another analysis in this chapter includes comparing results from the simulation to one of the analytical models describing the flame position to show that the model does not predict the Darreius Landau instability.

Contents

Nomenclature

Roman Symbols

$\mathscr{R}$	Specific gas constant	$[J/(kgK)]$
$\mathscr{V}$	Specific volume	$[m^3/kg]$
T	Temperature	$[k]$
$\dot{m}_f$	Fuel lass flow	$[kg/s]$
$\dot{Q}$	Global heat release flux	$[W]$
$\dot{q}$	Heat release flux per unit volume	$[W/m^3]$
$\mathscr{T}$	Oscillation period	$[s]$
A	Area	$[m^2]$
D_{th}	Thermal diffusivity	$[m^2/s]$
E	Density ratio	$[-]$
Fr	Froude number	$[-]$
g	Gravitational acceleration	$[m/s^2]$
H_f	Flame thickness at the base	$[m]$
H_u	Lower heating value	$[j/kg]$
k	Wave number	$[m^{-1}]$
L_f	Flame axial length	$[m]$
Ma	Markstein number	$[-]$
P	Pressure	$[Pa]$
Pr	Prandtl number	$[-]$

R	Characteristic flame length	$[m]$
S_L	Laminar flame speed	$[m/s]$
t	Time	$[s]$
U	Tangential velocity with respect to flame coordinates	$[m/s]$
u	Axial velocity	$[m/s]$
V	Normal-to-flame velocity with respect to flame coordinates	$[m/s]$
V	Volume	$[m^3]$
v_u	Unburnt gas inflow velocity	$[m/s]$

Greek Symbols

α	Flame angle	$[rad]$
δ	Thermal diffusion zone thickness	$[m]$
Λ	Air excess ratio	$[-]$
λ	Wave length	$[m]$
ν	Kinematic viscosity	$[m$š$/s]$
ω	Angular frequency	$[rad/S]$
ϕ	Equivalence ratio	$[-]$
ρ	Density	$[kg/m^3]$
σ	Temporal growth rate	$[s^{-1}]$
σ_x	Spatial growth rate	$[m^{-1}]$
τ	Flame transit time	$[s]$
θ	Reduced temperature	$[-]$
τ	Time delay	$[s]$
φ	Phase angle	$[rad]$
ξ	Flame position with respect to flame coordinates	$[m]$

Acronyms

FTF	Flame Transfer Function

1 Introduction

In many applications continuous combustion is the vital process that converts the chemical energy stored in the reactants into a useful thermal one, by which mechanical energy is produced by the means of one or more of the thermodynamic processes. Examples of these applications include thermal power generation stations, heating facilities and propulsion applications.

In a typical continuous combustion process, different dynamics are exhibited. One of which involves the flame interaction with the acoustic field, which result in self sustained oscillations of the flame. This kind of combustion oscillation, when uncontrolled, are accompanied by growth in heat release and pressure oscillations. These undesirable fluctuations does not only lead sometimes to high acoustic noise, but also mechanical damage inside the combustion chambers. It therefore remains one of the most challenging problems experienced by researchers and engineers in the field of combustion engineering. Before getting into technical detail, it might be interesting to get to know some facts about the history of combustion oscillations.

"A deaf man might have seen the harmony!", quoted by *Le Conte* in 1958 when he first discovered the "dancing flame" after observing the flame being pulsated with the audible music beats [13]. According to him, the trills of the musical instrument were perfectly reflected on the sheet of flame. Moreover, the "singing flame" was discovered by *Higgins* in 1977, which aroused the interest of other researchers who found that sound can be generated by having the flame in a larger tube diameter than that of the fuel supply tube, where the flame is anchored on [13].

While some of the researchers are focusing on the determination of the so called *Flame Transfer Function* by dealing with the combustion chamber as a black box that is exposed to acoustic perturbations and trying to analyze the system response by tracking its output, some others are more concerned with influence of these perturbations on the flame behavior. In this project, we are trying to work in both direction in parallel in order to find a connection between them.

In this thesis, we start by introducing the thermo-acoustic systems in as a simple model of several elements . We then focus on the flame and define the *Flame Transfer Function*. In the second part of chapter 2 we introduce the fundamental theories regarding the dynamics of laminar premixed flames. We then explain a field equation that describes the flame position. From this equation we introduce a general model that describes an inclined flame front displacement in 2D which makes us able to predict the effect of velocity perturbations. Moreover, we explain the flame instability and introduce two analytical models describing its growth rate. An analytical representation of the *FTF* is derived in chapter 3. We then review

the work of *Searby* [28] that includes the experimental determination of the Darrieus-Landau instability of V-Flames. Chapter 4 starts with describing the case being experimented. The geometry, mesh and boundary conditions are explained. This chapter ends by explaining the post processing technique.

Finally the results are included in chapter 5. We start by comparing the heat release perturbations in response to different excitation methods. We then discuss the gain and phase of the *FTF*. We switch afterwards to looking at the flame front behavior for different harmonic frequencies and analyze the one with highest instability, try to find the reason using an impulsive excitation test, with an attempt to draw a conclusion from the observed unusual behavior of the *FTF* and the flame dynamics. Further observations are then made with respect to the flame tip response. Another analysis in this chapter includes comparing results from the simulation to one of the analytical models explained in chapter 2.

2 Theoretical Background

Before going into details of thermo-acoustic systems, it could be useful to introduce some basics about the combustion process and the reason why industries prefer the use premixed combustion, which arises the appearance of thermo-acoustic problems.

Combustion

A gas turbine cycle might be an open or a closed one. In the latter a heat exchanger is used to transfer heat to the air. In the open-cycle unit the fuel is sprayed directly into the air in a continuous fashion [10], unlike that of the ICE where the combustion might be referred to as cyclic. There are mainly two types of continuous combustion systems for open cycles. In the first one, the compressed air coming from the compressor is divided into many streams where each one is supplied to separate cylindrical can-type combustion chamber. In the other one, the air flows from the compressor through an annular combustion chamber. In all of them, an electrical ignition normally initiates the combustion before the fuel starts to burn and the flame stabilizes [10].

The simplest continuous combustion process can be considered as a reacting mixture flowing in a straight-walled duct connecting the compressor and turbine with a flame anchored at a certain location in the duct. Ignition starts at the flame base leading to a release of heat out of the chemical energy stored in the reactants, eventually the temperature is raised and density is lowered [13].However, the high pressure drop of this design makes it undesirable (the pressure drop from combustion is proportional to the square of the air velocity [15]). One idea in order to avoid this excessive pressure drop to an acceptable level is to install a diffuser. But in this case, the air velocity might still be too high to allow stable combustion [15]. Engineers therefore came up with the idea of installing a baffle to anchor a flame; look Fig. 2.1. In this case, a low velocity region is acquired after the baffle. An eddy region is namely formed behind the baffle that draws the gases in for complete combustion. This steady circulation of the flow stabilizes the flame and provides continuous ignition.

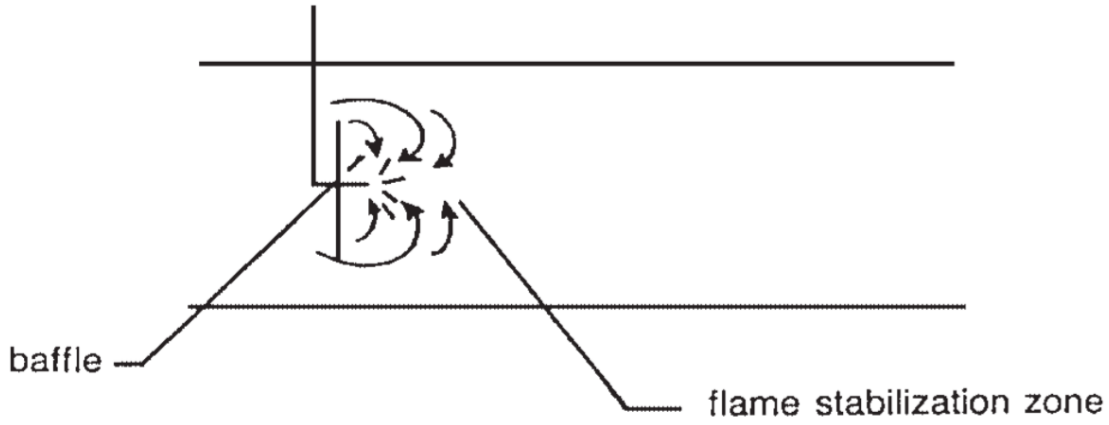

Figure 2.1: Flame stabilized using a baffle to form an eddy region [15].

Natural gas (methane) is a carbohydrate fuel that is very commonly used in gas turbines. The products of methane are normally carbon dioxide and water.

$$CH_4 + 2O_2 \longrightarrow CO_2 + 2H_2O + heat \tag{2.1}$$

However, pure oxygen is not normally used in combustion processes, but air is used instead. Since that air consists of 21% Oxygen and 79% nitrogen, nitrogen is involved with a considerable amount (as four times as oxygen) in the reaction of methane. The complete combustion of methane therefore is

$$1CH_4 + 2(O_2 + 4N_2) \longrightarrow 1CO_2 + 8N_2 + 8H_2O + heat \tag{2.2}$$

which means that in order to burn $1m^3$ of methane we essentially need $2m^3$ of oxygen and $8m^3$ of nitrogen. Furthermore, during the combustion process, a secondary chemical reaction occurs that leads to the formation of nitric acid. That is

$$2N + 5O + H_2O \longrightarrow 2NO + 3O + H_2O \longrightarrow 2HNO \tag{2.3}$$

From reaction (2.3) we can deduce that the formation of nitric acid can is dependent on the that of nitric oxide.

Of all the emission products from a combustor, NO_x are of special interest due to its particular behavior in air as pollutant [14]. It combines with O_2 to form ozone in the lower atmosphere; which is very harmful for living organisms. If released in the upper atmosphere, NO_x causes depletion of the ozone layer; having the Ozone in the Stratosphere is very important as it prevents intense UV rays from entering into the Earth's atmosphere. Furthermore, NO_x together with SO_x are responsible for the formation of acid rain. These reasons together with the rising public awareness have led more strict regulations on the emission levels all around the globe [12].

Fig. 2.2 shows the variation of different emissions with varying equivalence ratios. It could be seen that the NOx levels are maximum at air to fuel ratio just below the stoichiometric

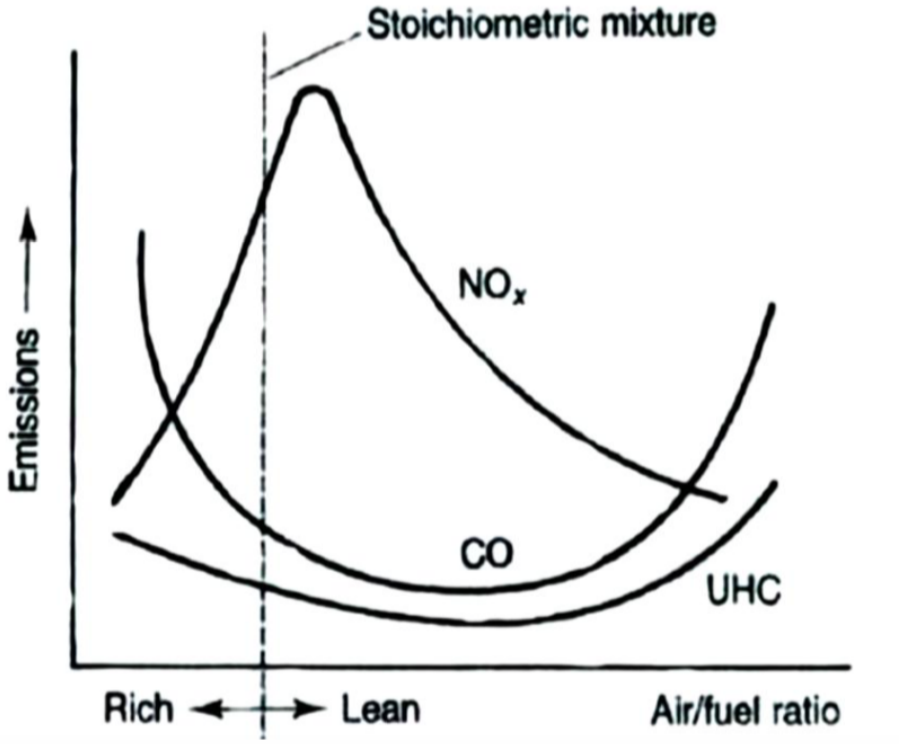

Figure 2.2: Emission production vs equivalence ratio [14].

ratio [14]. Moreover, rich mixtures are unfavorable due to less efficiency and incomplete combustion that leads to other poisonous products like carbon monoxides. Furthermore, Formation of NO_x depends exponentially on the (local) temperature in the combustion zone [25]; see Fig. 2.3. Therefore, keeping a uniform low temperature in the reaction zone would be in favor of low emission. Engineers have proposed several methods to control NO_x emissions, whey can be divided into two main categories; dry and wet methods. The latter deals with injecting liquids upstream of the combustion process in order to lower the peak temperature inside the combustion chamber; demineralised water is commonly used [14]. Dry Methods incorporate certain design changes to the combustor which would result in lower emissions. These changes might be either in geometry of combustors, the fuel scheduling of or in the of utilization of the air fed into the combustion chamber. One of those methods deals with minimizing the peak flame temperature by operating with a very lean primary zone. This method is referred to as *Lean Pre-mixed Pre-vaporised* or LPP. The combination of a lean premixed flame and convectively cooled combustion chambers has led to the rise of another problem: combustion driven oscillations, or thermoacoustic instabilities. The absence of by-pass air in convectively cooled combustion systems results in a decrease of acoustic damping and hence an increase in pulsation amplitudes. The mechanism of thermoacoustic instabilities due to premixed flames will be discussed in this work. [25]

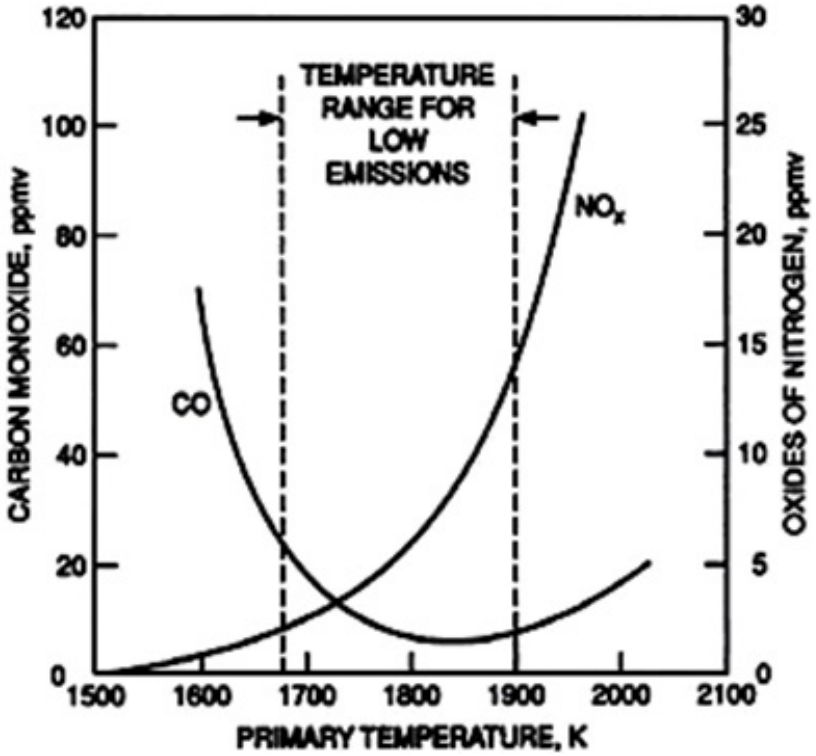

Figure 2.3: Emission production vs temperature [14].

2.1 Combustion Instabilities

Thermoacoustic instabilities are self-sustained oscillations that originate from a coupling between any kind of heat transfer or heat release and the acoustics of a technical system [12]. If the heat release is generated by a flame, the oscillation is called a combustion instability.

Acoustic perturbations affects the flame by fluctuating the heat release, this implies a fluctuation in the volumetric expansion and eventually a generation of sound wave [12] The flame reacts to an acoustic perturbation by a fluctuation of the heat release and thus a fluctuation of the volumetric expansion that in turn is nothing else but a sound wave. That sound wave propagates through the combustor, is reflected at the boundaries and propagates back to the flame, where it again causes an acoustic perturbation. This feedback is essential and leads - for favourable conditions - to an amplification of the perturbation for every repetition of the cycle. Without feedback, the flame acts just as a once-through amplifier of turbulent noise and coherent vortex structures

Combustion chambers can be viewed as organ pipes in which acoustic pressure and velocity oscillations can be sustained. Flames, which are essentially surfaces across which reactants are converted into products, not only possess their own inherent instabilities, but are also known to respond readily to imposed fluctuations. The potential coupling between the unsteady components of pressure and heat release rate can lead to their resonant coupling, thus growth, an is referred to as thermoacoustic instability. [13]

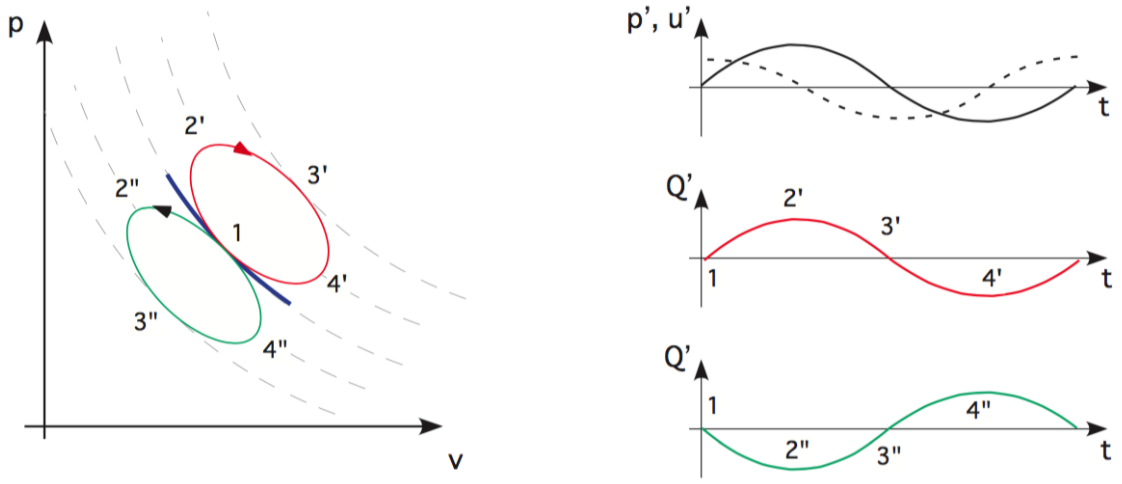

Figure 2.4: Thermodynamic analogy of Rayleigh criterion [22]. Left: p-v diagram of isentropic compression / expansion, with heat addition in-phase with pressure fluctuations (1-2'-3'-4') and out-of phase (1-2"-3"-4"). The dashed gray lines represent lines of constant entropy. Right-top: Fluctuations of pressure (—) and velocity (- -). Right-middle/bottom: in-phase / out-of-phase fluctuations of heat release rate.

Rijke showed that sound can be generated in a vertical tube open at both ends by placing a heated metal gauze inside the tube. The sound was heard only when the heating element was placed in the lower half of the tube, specifically at a distance of a quarter the tube length from the bottom. [13]

The Rayleigh Stability Criterion

In 1878 Rayleigh was the first to set a hypothesis for combustion instability and propose a criterion that explains energy transfer to the acoustic oscillation. It states that for instability to occur, heat must be released at the moment of greatest compression [22]. That is, if the pressure fluctuation is in phase with the heat release fluctuation, acoustic energy will be generated that will be greater than the lost energy, eventually a less stable system would be observed. On the other hand, if the pressure fluctuation and heat release are out of phase, the oscillations will tend to damp (vibration discouraged).

In general, the mathematical formula of the Rayleigh criterion can be represented in this inequality by taking the integration over time and volume [13]

$$\int_0^V \int_0^T \dot{q}'(t,V) \cdot p'(t,V)\, dt\, dV > \int_0^V \int_0^T \Psi(t,V)\, dt\, dV \tag{2.4}$$

where the notations p', $\dot{q}'$ and Ψ stand for pressure perturbations,heat release perturbations and wave energy dissipation, respectively. Whilst the integral runs over one oscillation period T inside the control volume V.

The LHS term of Eq. (2.4) describes the energy added to the oscillation per one cycle due to heat addition process. On this side of the equation, for acoustically compact flames (the flame extension is much smaller than the acoustic wavelength), the pressure perturbation term reduces to $p'(t)$ [12]. Moreover, the energy dissipated (RHS of Eq. (2.4)) can be assumed very small (RHS~0) [13]. The Rayleigh criterion can then be given in it's simplest form [12]

$$\int_0^T \dot{Q}'(t) \cdot p'(t)\, dt > 0 \tag{2.5}$$

with

$$\dot{Q}'(t) = \int_0^V \dot{q}'(t, V)\, dV. \tag{2.6}$$

Researchers had came up with an analogy that enables us to perceive this criterion as a thermodynamic cycle of a piston engine. However, in this case compression and expansion is achieved by the means of a standing acoustic wave [22]. Further, due to the fact that sound waves are isentropic, change in volume will be made at a constant line of entropy. Now consider heat added periodically to an ideal gas inside a control volume such that

$$\mathcal{V} = \frac{\mathscr{R}T}{PM} \tag{2.7}$$

with $\mathscr{R}$ being the specific gas constant, P the pressure and M is the total mass within the control volume. According to Eq. (2.7) this will result in an increase in the specific volume. If this happens at the point of maximum pressure, a clockwise cycle will be initiated, resulting in increase of the oscillation energy that might lead to a self-excited instability; see Fig. 2.4. This is exactly what happens when a piston is at the top dead center (TDC), the engine delivers the maximum work.

On the other hand, if heat is added at a point where maximum pressure is not yet reached, the cycle efficiency will decrease and less energy will be added to the oscillation. In the case where heat is added at the point of minimum pressure, this will initiate a counterclockwise cycle (1- 2"- 3"- 4") and energy will be extracted from the oscillation leading to damping. Using the same piston engine analogy, if heat is added where piston is at BDC, the engine will slow down.

2.2 Stability Analysis

2.2.1 Network Modeling

Complex thermo-acoustic systems can be reduced into a simpler network of acoustic elements to reduce its complexity. With each element corresponding to a specific component of the system. Those elements might include for example ducts, nozzles, burners, flames and/or boundary conditions for system termination as shown in Fig. 2.5. For a linear acoustic system, a low order model might be established in a simple way. System elements might be connected together via the Fourier-transformed fluctuations of the acoustic variables pressure p'

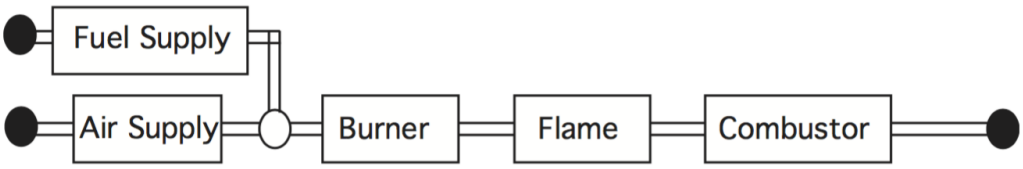

Figure 2.5: Network model of a simple combustion system [22].

and velocity u'. However, a conversion between those variables and equivalent notations, referred to as *Riemann invariants* is possible. Those alternative invariants are denoted as f and g and they represent downstream and upstream propagating acoustic waves [25] [12]. Once all the elements are defined, control theory derived methods could be applied to solve the system [24]

In combustion systems, the flame is one element that is included in the network model. However, the detailed knowledge about fluctuations effects on the flame is still not very well understandable [12]. For this reason several approaches including experimental, numerical and analytical ones are often employed to characterize the flame response in order to define the appropriate element to be inserted into the low order model. In general they can be categorized into two methods: The *Transfer Matrix* method and the *Flame Transfer Function* method. Since that within the context of this work we are more interested in the latter, therefore we are going to focus on it

2.2.2 Flames Transfer Function

A Flame behavior could be characterised by a function that relates the upstream velocity fluctuations u' to the total heat release fluctuations $\dot{Q}'$. This is known as the *Flame Transfer Function (FTF)*. Its mathematical relation states [12]

$$FTF = \frac{\dot{Q}'/\overline{\dot{Q}}}{u'/\overline{u}} \tag{2.8}$$

where $\overline{\dot{Q}}$ and $\overline{u}$ are the mean values of the global heat release and the upstream velocity respectively. However, this behavior depends on the oscillation frequency and therefore a Fourier-transformation is usually applied to Eq. (2.8) to convert it into the frequency domain. This results is Eq. (2.9)

$$FTF(\omega) = \frac{\dot{Q}'(\omega)/\overline{\dot{Q}}}{u'(\omega)/\overline{u}} \tag{2.9}$$

where $FTF(\omega)$ is the flame transfer function defined at the complex perturbations $\dot{Q}'(\omega)$ and $\dot{u}'(\omega)$ of frequency ω.

For a sinusoidal harmonic input represented in the complex plane, the heat release and

velocity fluctuation could be represented as

$$\begin{aligned} \dot{Q}'(\omega) &= \hat{\dot{Q}}(\omega) e^{i\omega t + i\varphi_{\dot{Q}}(\omega)} \\ u'(\omega) &= \hat{u}(\omega) e^{i\omega t + i\varphi_u(\omega)} \end{aligned} \tag{2.10}$$

whereas $\hat{\dot{Q}}(\omega)$ and $\hat{u}$ denote the amplitudes of heat release and velocity while $\varphi_{\dot{Q}}(\omega)$ and $\varphi_u(\omega)$ are their phase angles. By substituting (2.10) into (2.9) the Flame Transfer Function could be given in terms of amplitudes and phase angles as

$$FTF(\omega) = \frac{\hat{\dot{Q}}(\omega)}{\hat{u}(\omega)} \frac{\overline{u}}{\overline{\dot{Q}}} e^{i[\varphi_{\dot{Q}}(\omega) - \varphi_u(\omega)]} \tag{2.11}$$

Eq. (2.11) explicitly defines the amplitude and phase of the transfer function in terms of input and output signals, thus we can deduce that the gain and phase shift are given as

$$\begin{aligned} \widehat{FTF}(\omega) &= \frac{\hat{\dot{Q}}(\omega)}{\hat{u}(\omega)} \frac{\overline{u}}{\overline{\dot{Q}}} \\ \varphi_{FTF}(\omega) &= \varphi_{\dot{Q}}(\omega) - \varphi_u(\omega) \end{aligned} \tag{2.12}$$

A time delay τ is usually observed in the heat release response to the velocity perturbation. That is the instantaneous heat release fluctuation at time t would be the response to that of the velocity at time $(t-\tau)$. This characteristic appears in the transfer function so that Eq. (2.8) writes

$$FTF = \frac{\dot{Q}'(t)/\overline{\dot{Q}}}{u'(t-\tau)/\overline{u}}. \tag{2.13}$$

Convective characteristics, that depend on the flow velocity, are usually the main source of the time delay appearing in Eq. (2.13). Assuming a zero phase reference in Eq. (2.12) such that $\varphi_u = 0$ and considering the time delay in the heat release phase so that $\varphi_{\dot{Q}} = -\omega\tau$. With $\omega = 2\pi/\mathcal{T}$, where $\mathcal{T}$ is the oscillation period, the phase shift of the *Flame Transfer Function* is then given by

$$\varphi_{FTF}(\omega) = -2\pi \frac{\tau}{\mathcal{T}} \tag{2.14}$$

which means that with an increasing excitation frequency, decreasing $\mathcal{T}$, the more the time delay τ is the steeper the negative gradient of $\varphi_{FTF}(\omega)$. It could be concluded that since τ controls the heat release phase, it could have a remarkable effect on the combustion stability according to Reyleigh's criterion which is represented by Eq. (2.5) [12]

Considering an ideal homogeneous premixed mixture that does not have any nonuniformity neither in space nor in time, the system response in a low frequency limit should be equal to one. In other words, velocity fluctuations should translate into heat release fluctuations that is

$$\frac{\hat{u}(\omega)}{\overline{u}} = \frac{\hat{\dot{Q}}(\omega)}{\overline{\dot{Q}}} \tag{2.15}$$

for

$$\lim_{\omega \to 0} \widehat{FTF}(\omega) = 1 \tag{2.16}$$

And for a time delay that is much smaller than the oscillation period $\tau \ll \mathcal{T}$, one can deduce from Eq. (2.14)

$$\lim_{\omega \to 0} \varphi_{FTF}(\omega) = 0 \tag{2.17}$$

As the frequency increases, the flame starts to lose its ability to capture the perturbations and eventually the gain of the *FTF* starts to decrease

$$\lim_{\omega \to \infty} \widehat{FTF}(\omega) = 0 \tag{2.18}$$

However, researchers have found that often intermediate frequencies have the tendency to give an amplitude peak higher than unity.

2.3 Flame dynamics

A transfer function correlates the heat release perturbations to the modulations of the gas velocity. Since that the heat release perturbation $\dot{Q}'$ is assumed proportional to that of the flame area A' (this will be explained in the next chapter), the prediction of the flame area becomes necessary and for this we need to understand the flame dynamics.

2.3.1 Flame Front Kinematics

Bunsen burners are often used to generate laminar premixed flames. With a Bunsen burner, it is possible to control the velocity as well as the equivalence ratio of the jet entering into the combustion chamber. The fuel enters with high momentum through the orifice which leads to an underpressure that entrains air into the tube, which is then mixed with the fuel to generate a homogeneous premixed mixture at the exit.

Flame Structure

In Fig. 2.6 a schematic representation of the flame structure is shown. If we consider that the steady state case is normal to the x-direction where the unburnt mixture is on the left side of the reaction zone and the burnt mixture on its right. The fuel and oxidizer are convected from upstream with a burning velocity S_L and diffuse into the reaction zone. The products increase during the chemical reaction from Y_0 to $Y_{P,b}$ and simultaneously release the heat which leads to this temperature rise from T_u to T_b in the reaction zone. However, due to concentration difference, the products diffuse upstream and get mixed with the fresh mixture. In a similar fashion, the heat is also conducted due to temperature difference between the two zones leading to the preheat zone. As soon as the inner temperature layer is reached fuel is consumed and the temperature gradient increases. By the end of the reaction zone the fuel is entirely depleted and the remaining oxygen is convected downstream [21]

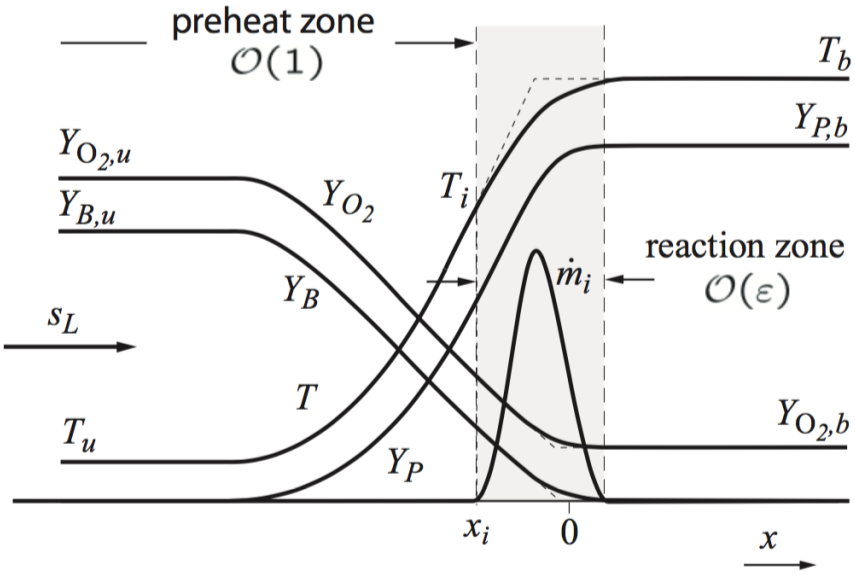

Figure 2.6: Flame structure of premixed laminar flame [20].

The Kinematic Balance

In steady state the velocity component normal to the flame front is locally equal to the flame front propagation velocity or the *laminar burning velocity* S_L which could be defined as the velocity of the flame normal to the flame front and relative to the unburnt mixture [21]. Now suppose that we know the unburnt gas inflow velocity v_u as well as the flame angle α. By splitting v_u into two components $v_{n,u}$, which is normal to the flame front, and $v_{n,t}$, the tangential component. The velocity balance in the normal component direction yields the relation

$$S_L = v_{n,u} = v_u \sin\alpha \tag{2.19}$$

Due to the large temperature gradient at the flame front, together with a constant pressure, a dramatic decrease in the density happens. This thermal expansion at the flame front leads to an increase in the normal velocity due to the mass balance between before and after the front. However, the tangential component remains the same. Vector addition of the components on the burnt gas side leads to a deflected resultant vector v_b from the direction of the burnt mixture. An illustration of the deflected streamlines is shown in Fig 2.8

$$\begin{aligned} v_{n,b} &= v_{n,u}\frac{\rho_u}{\rho_b} \\ v_{t,b} &= v_{t,u} \end{aligned} \tag{2.20}$$

The tip of the flame usually experiences a special condition. Since that it is located at the symmetry line, the tangential component becomes zero and the burning velocity becomes only equal to the normal component of the burnt side. This increasing the tip burning velocity by a factor of $(1/\sin\alpha)$ over that of the oblique parts. This is well explained by a strong curvature

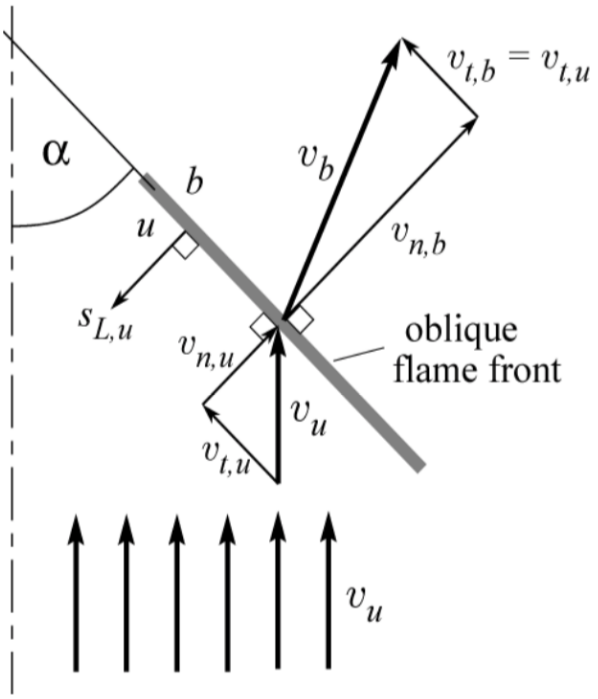

Figure 2.7: The kinematic balance of a steady oblique flame [21].

happening at the tip which leads to an increased preheating by the lateral parts (in addition to the preheating by conduction from the burnt side) [21] [20].

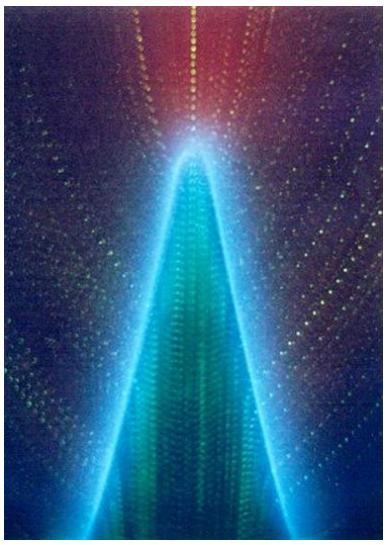

Figure 2.8: Laminar Bunsen flame [11].

Another experimental device that is used to measure laminar burning velocities is the spherical combustion vessel. In this one the flame is initiated by a spark at the center of the vessel where it starts to propagate on a radial shape. The propagation velocity then can be defined as the temporal rate of change in the radial displacement or dr_f/dt and the kinematic balance between the propagation velocity, flow velocity v_u and the burning velocity S_L could be given by [20]

$$\frac{dr_f}{dt} = v_u + S_{L,u} \tag{2.21}$$

2.3.2 Level Set Approach

The surface of the flame front can be described as the G_0-level set of a scalar function G (e.g., the temperature). Choosing as initial position a stationary position of the flamevfront, G is initialised on the grid by applying the signed distance function. A generalization of the kinematic relation (2.21) explained above is possible if one is to introduce a vector $\boldsymbol{n}$ which is normal to the flame front [21], it gives

$$\frac{d\boldsymbol{x}_f}{dt} = \boldsymbol{v} + s_L\boldsymbol{n} \tag{2.22}$$

with the vector $\boldsymbol{x}_f$ describing the flame position, $\frac{d\boldsymbol{x}_f}{dt}$ is therefore its propagation velocity and $\boldsymbol{v}$ the velocity vector. If one is to define a spatiotemporal varying function $G(x,t)$ where it represents a certain scalar field (e.g. the temperature) [19]. Consider the surface of the front to be described as the zero-level set of this scalar function or

$$G(x,t) = G_0 \tag{2.23}$$

where G_0 arbitrarily represents a stationary position of the surface. And the flame contour $G(x,t) = G_0$ divides the physical field into a region burnt gas where $G > G_0$ and another re-

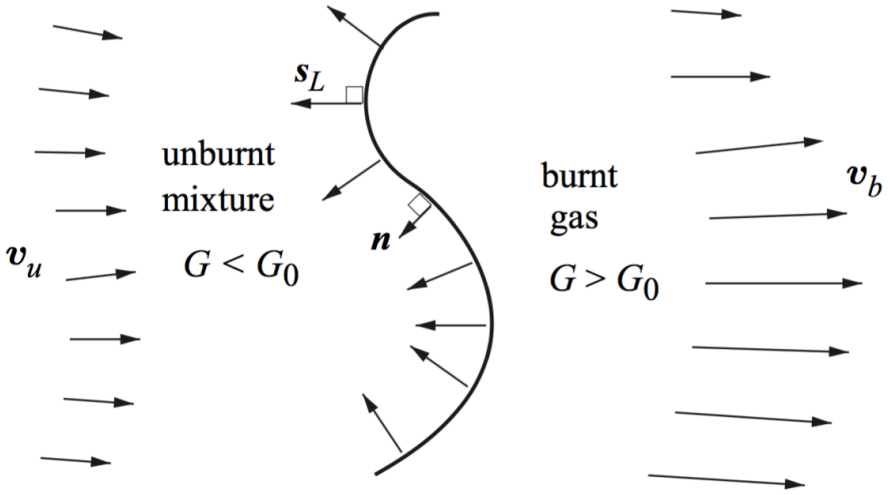

Figure 2.9: Propagating flame front [20].

gion of unburnt mixture where $G < G_0$. Then the normal vector pointing towards the unburnt mixture is then given by

$$\boldsymbol{n} = -\frac{\nabla G}{\nabla G} \tag{2.24}$$

By differentiating Eq. (2.23) with respect to t at $G = G_0$ one obtains

$$\frac{\partial G}{\partial T} + \nabla G \cdot \frac{d\boldsymbol{x}}{dt}\Big|_{G=G_0} = 0 \tag{2.25}$$

Now by substituting Eq. (2.22), Eq. (2.24) into Eq. (2.25) leads to the field equation, or the $G-Equation$

$$\frac{\partial G}{\partial T} + \boldsymbol{v}\nabla G = s_L|\nabla G| \tag{2.26}$$

2.3.3 Inclined Flame Model

If one is to recall the G-equation (2.26) in a two-dimensional velocity field it becomes

$$\frac{\partial G}{\partial t} + u\frac{\partial G}{\partial x} + v\frac{\partial G}{\partial y} = S_L\left[\left(\frac{\partial G}{\partial x}\right)^2 + \left(\frac{\partial G}{\partial y}\right)^2\right]^{1/2} \tag{2.27}$$

Now consider an inclined flame anchored at the origin as in Fig. 2.10 such that, in the laboratory reference flame (x, y), the uniform mean flow velocity is $\overline{\boldsymbol{u}} = (0, v)$ and the steady flame position is given by $G_0 = y - \overline{\eta}(x) = 0$. The flame position from Eq. (2.27) is then given by [27]

$$\overline{\eta}(x) = \frac{x}{\sqrt{\left(\frac{v}{S_L}\right)^2 - 1}} = \frac{x}{\tan\alpha} \tag{2.28}$$

If the incident velocity field is exposed to a small perturbation so that (0, v) becomes (u', v+v') with u' and v' being much smaller than the mean flow velocity. As suggested by Boyer and Quinard [4], let (X, Y) be a new coordinate system aligned to the inclined flame. With respect to this coordinate system the perturbed flame position could be represented as

$$G = Y - \xi(X,t) = 0 \tag{2.29}$$

and the respective velocity components could be introduced as

$$\begin{aligned} \overline{U} &= v\cos\alpha \\ \overline{V} &= v\sin\alpha \end{aligned} \tag{2.30}$$

Now Eq. (2.27) could be reformulated with respect to the new frame of reference as [27]

$$\frac{\partial\xi}{\partial t} - V + U\frac{\partial\xi}{\partial X} = -S_L\left[1+\left(\frac{\partial\xi}{\partial X}\right)^2\right]^{1/2} \tag{2.31}$$

with U and V being the tangential and normal to flame front velocity components

$$\begin{aligned} U &= \overline{U} + U' \\ V &= \overline{V} + V' \end{aligned} \tag{2.32}$$

while the tangential and normal to flame front flow perturbations are

$$\begin{aligned} U' &= v'\cos\alpha + u'\sin\alpha \\ V' &= v'\sin\alpha - u'\cos\alpha \end{aligned} \tag{2.33}$$

It could be then deduced that to first order in perturbations Eq. (2.31) yields

$$\frac{\partial\xi}{\partial t} + (\overline{U} + U')\frac{\partial\xi}{\partial X} = \overline{V} - S_L + V' \tag{2.34}$$

By balancing the velocity components of the Y axis normal to the flame, we find that V' and S_L cancel each other out. In addition U' could be neglected since $U' << \overline{U}$ and Eq. (2.34) finally becomes

$$V'(X,t) = \frac{\partial\xi}{\partial t} + \overline{U}\frac{\partial\xi}{\partial X} \tag{2.35}$$

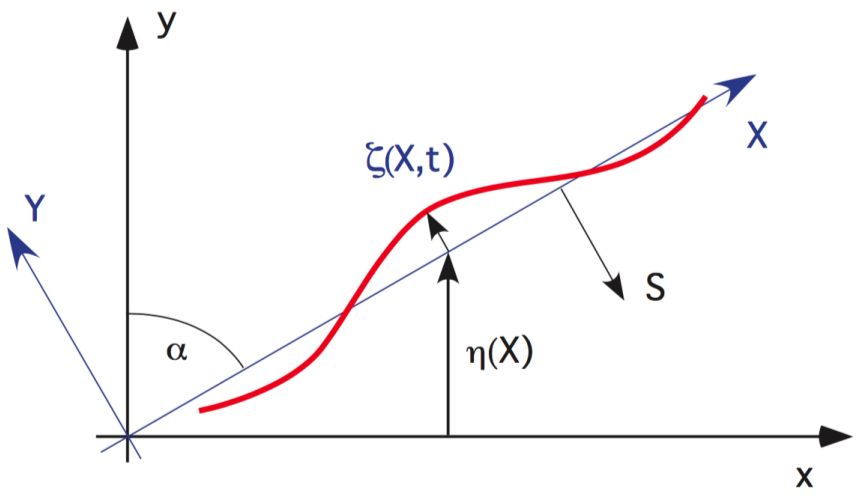

Figure 2.10: An inclined flame sheet with (x, y) being the laboratory reference frame and (X, Y) the flame aligned reference frame [22].

Eq. (2.35) tells us that in the steady state the flame front propagation S_L balances the normal to flame front velocity V. However, this balance could be disturbed ($V' \neq 0$) in two ways, either by a direct change of the flame front position at location X in time t or by a convected wrinkle along the flame front, such that $\partial\xi/\partial X \neq 0$, with velocity $\overline{U}$ [22].

The solution of the first order kinematic Eq. (2.35) yields to

$$\xi(X,t) = \frac{1}{\overline{U}} \int_0^X V'\left(X', t - \frac{X - X'}{\overline{U}}\right) dX' \tag{2.36}$$

According to Polifke [22], this equation tells us a very interesting fact which is that the disturbed flame front position is not only affected by the current velocity perturbations V', but also by earlier perturbations that appeared upstream at position $X - X'$ and have been convected along the flame front with velocity U to the present position X. The integral in Eq. (2.36) is therefore considers not only the instantaneous flame behavior, but it takes into account the history of the perturbations. This makes us think back to the importance of time delays in combustion stability, that have been mentioned in Sec. 2.2.2, as they influence the phase shift between excited perturbations and heat release in response to this excitation.

By considering time harmonic perturbations such that $V'(X,t) = \widetilde{V}(X)e^{-i\omega t}$ eventually the flame displacement becomes also harmonic $\xi(X,t) = \widetilde{\xi}(X)e^{-i\omega t}$ and Eq. (2.36) writes

$$\widetilde{\xi}(X) = e^{i\omega\frac{X}{\overline{U}}} \frac{1}{\overline{U}} \int_0^X \widetilde{V}(X')e^{-i\omega\frac{X'}{\overline{U}}} dX' \tag{2.37}$$

Velocity Perturbations

Until here we have been talking about the flame displacement and how it might respond to a harmonic perturbation. However we have not mentioned exactly what kind of this pertur-

bation could be. We here are going to discuss two approaches of modeling velocity modulations; *Uniform velocity perturbation* and *axial convective wave*. While the former deals with confined combustion systems where the flame length L is much shorter than the wavelength λ, the latter considers unconfined cases where the flame is long enough to observe the convected disturbances along the flame front.

In the modeling of *uniform velocity perturbation* the flame is considered compact and a harmonic and spatially homogeneous velocity modulation on the flame front is expressed by

$$u' = 0, v' = v_1 e^{-i\omega t} \tag{2.38}$$

By substitution of Eq. (2.38) into the harmonic displacement $\widetilde{\xi}$ Eq. (2.37), after converting it to the laboratory frame reference and variables, it yields

$$\frac{\widetilde{\xi}(X)\cos\alpha}{R} = \frac{v_1}{\bar{v}}\frac{1}{i\omega_*}\left[e^{i\omega_* \frac{x}{R}} - 1\right] \tag{2.39}$$

which appears to depend solely on the reduced frequency, $\omega_* = (\omega R)/S_L \cos\alpha$, with R being the flame extension along the x-axis [22]. This representation is a fairly good approximation of the flame displacement in the low frequency limit, i.e. as long as the wavelength λ is larger than the characteristic scale R [27].

On the other hand, at relatively high frequencies the *axial convective wave* modeling approach is more appropriate as it considers the upstream velocity modulations to be convected in the axial direction and eventually also along the flame front. With the wave number $k = \omega/\bar{v}$ the velocity propagation in the y direction of the laboratory frame is given by

$$u' = 0, v' = v_1 e^{iky - i\omega t} \tag{2.40}$$

Again by substituting this into the harmonic displacement Eq. (2.37) in the laboratory coordinates it gives us

$$\frac{\widetilde{\xi}(X)\cos\alpha}{R} = \frac{v_1}{\bar{v}}\frac{1}{i\omega_*}\frac{1}{1-\cos^2\alpha}\left[e^{i\omega_* \frac{x}{R}} - e^{i\omega_* \frac{x}{R}\cos^2\alpha}\right] \tag{2.41}$$

which makes the flame displacement now depend on a second parameter, which is the flame angle α, in addition to the reduced frequency ω_*, which has already been seen in the first approach as well.

It worth noting here that both expressions from the two models coincide as the flame angle α approaches $\pi/2$, or in the limit of $\cos\alpha \to 0$. The interpretation of this is that if the flame becomes normal to the flow direction, it acts as if it is subjected to a uniform velocity perturbation. In general, the flame displacement expression given by the second approach, Eq. (2.41), contains the expression from Eq. (2.39) and is expected to give more realistic results at high as well as low frequencies. Both models are a good start point for an analytical derivation of the *Flame Transfer Function* which will be discussed in chapter 3.

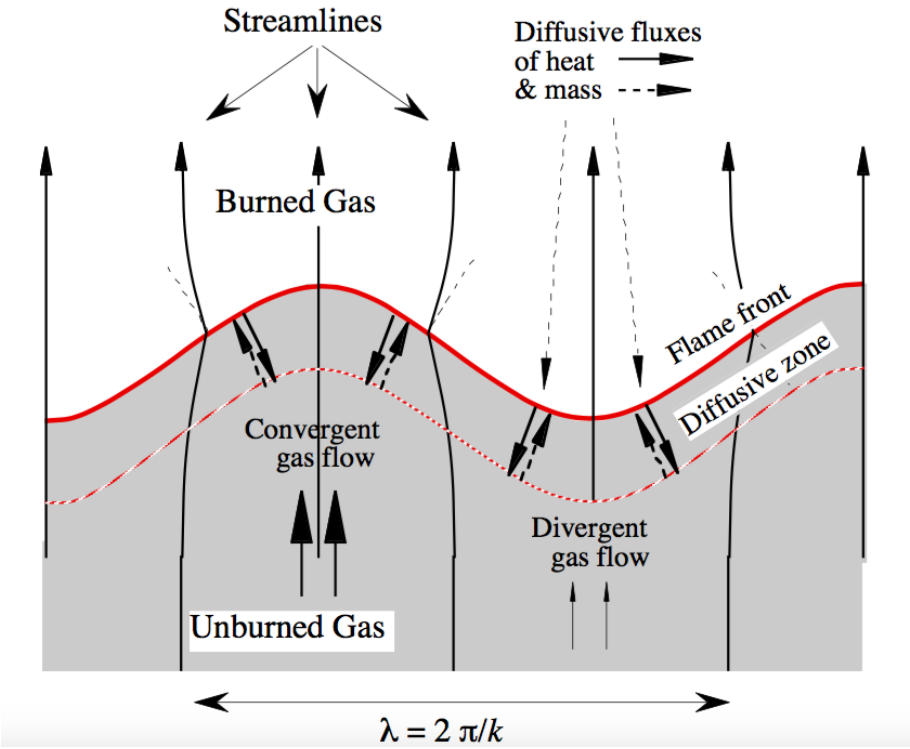

Figure 2.11: Wrinkling of flame front showing the hydrodynamics of streamlines and diffusive fluxes of heat and mass [26].

2.3.4 Instability in Premixed Combustion

Flame instability can appear in different forms and scales. Two main types of instability are referred to as hydrodynamic instabilities and thermal-diffusive instabilities. The former type is mainly a result of thermal expansion and is the dominant one in case of premixed flames. It is the major cause of sharp folds and creases that could be seen in the flame front and for the wrinkles observed at the surface of expanding flames. On the other hand, diffusion flames are more affected by the thermal-diffusive type on instability with thermal expansion playing a secondary role [18]. Since that this thesis is more concerned with premixed laminar flames, we are not going to talk in detail about the latter.

Darrieus(1938) had first discovered the hydrodynamic instability due to the thermal gas expansion. With the flame being considered as a thin interface propagating towards the fresh gas with a constant speed S_L, he found that the heat release in a wrinkled premixed flame will lead to gas expansion that will deviate flow lines across the front towards the normal to the flame. Considering the incompressibility of the flame due to the low Mach number, the upstream lines are also deviated; Fig. 2.11. This would lead to flow divergence that would result in velocity and pressure gradients and increases the flame wrinkling [28] [6].

Planar flames were predicted to be unconditionally unstable at all wavelengths later on by Landau(1994). Considering only the gas expansion, he approximated the wrinkling growth

rate to be [26]

$$\sigma = k \cdot S_L \frac{E}{E+1} \cdot \left(\sqrt{\frac{E^2+E-1}{E}} - 1 \right) \tag{2.42}$$

where k is the perturbation wave number and E is the gas expansion ratio between the fresh and burnt gas sides, which is the same as the inverse of the temperature ratio

$$E = \frac{\rho_u}{\rho_b} = \frac{T_b}{T_a}. \tag{2.43}$$

Clavin and Garcia [8] have derived a more complicated dispersion relation. The took into account the influences of the flame front acceleration, the preferential diffusion as well as the temperature dependent diffusion coefficients. Their dispersion relation for the amplitude of small perturbations is governed by the second order equation:

$$(\sigma\tau_t)^2 A(k) + \sigma\tau_t B(k) + C(k) = 0. \tag{2.44}$$

Note that, for the sake of notation consistency with the rest of the text, Eq. (2.44) is taken not from the original work by Clavin and Garcia [8] but rather from the theoretical review done by Traffaut and Searby [28]. In this equation, the growth rate is represented in the real part of σ while τ_t represents the flame transit time and is given by

$$\begin{aligned} \tau &= \frac{\delta}{S_L} \\ \delta &= \frac{D_{\text{th}}}{S_L} \end{aligned} \tag{2.45}$$

where δ and D_{th} are thermal diffusion zone thickness and the thermal diffusivity, respectively. The wave number dependent coefficients are mathematically defined as

$$\begin{aligned} A(k) &= \frac{E+1}{E} + \frac{E-1}{E} k\delta \left(Ma - J\frac{E}{E-1} \right) \\ B(k) &= 2k\delta + 2E(k\delta)^2 (Ma - J) \\ C(k) &= \frac{E-1}{E}\frac{k\delta}{Fr} - (E-1)(k\delta)^2 \left[1 + \frac{1}{EFr}\left(Ma - J\frac{E}{E-1} \right) \right] \\ &+ (E-1)(k\delta)^3 \left[h_b + \frac{3E-1}{E-1} Ma - \frac{E}{E-1} 2J + (2Pr-1)H \right] \end{aligned} \tag{2.46}$$

while the coefficients H and J account for the diffusivity dependence on the temperature and are represented in the integrals

$$\begin{aligned} H &= \int_0^1 h_b - h(\theta)\, d\theta \\ J &= (E-1) \int_0^1 \frac{h(\theta)}{1 + (E-1)\theta}\, d\theta \end{aligned} \tag{2.47}$$

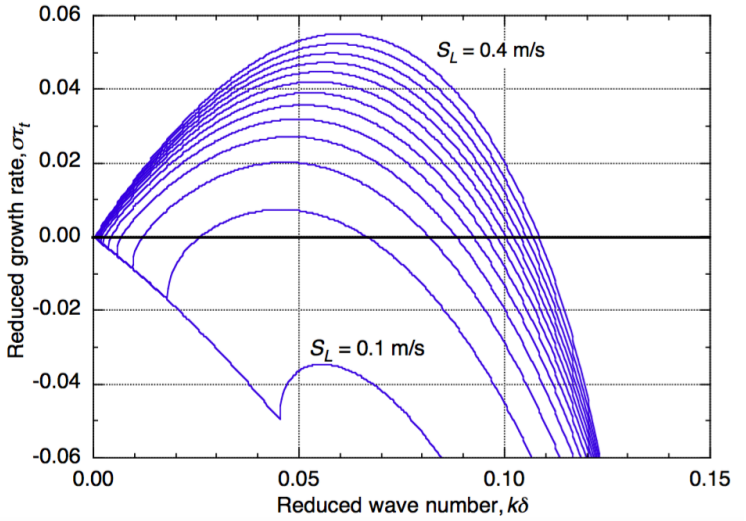

Figure 2.12: Reduced growth rate of Darrieus-Landau instability plotted as a function of reduced wavenumber for different flame speeds [26].

with the reduced temperature θ and $h(\theta)$ are given in terms of the real temperature T, the density ρ and the thermal diffusivity D_{th} by

$$\begin{aligned} \theta &= \frac{T - T_u}{T_b - T_u} \\ h(\theta) &= \rho D_{\text{th}}. \end{aligned} \tag{2.48}$$

Left out are the three constants Fr, Pr and Ma and they represent the Froude number, Prandtl number and the Markstein number, respectively. The first two are given by

$$\begin{aligned} Fr &= \frac{S_L^2}{g\delta} \\ Pr &= \frac{\nu}{D_{\text{th}}} \end{aligned} \tag{2.49}$$

where g is the gravitational acceleration and ν is the momentum diffusivity. Last is the Markstein number, which describes the effects of curvature and stretch on the local burning velocity. Markstein numbers are normally obtainable from experimental measurements or numerical simulations. However, a rough estimation has also been given by Clavin and Garcia [8]. With β stands for the Zel'dovich number, the Markstein number is given by

$$Ma = \frac{E}{E-1} J + \frac{\beta}{2} \int_0^1 \frac{h(\theta) ln(\theta^{-1})}{1 + (E-1)\theta} d\theta \tag{2.50}$$

A positive Ma means that preferential diffusion reduces the growth rate of the hydrodynamic instability at large wave numbers. In other words, the curvature effect decreases the

burning velocity of a region that is convex towards the fresh gas side, thus the flame is thermo-diffusively stable [26]. This leads to a growth rate peak appearing at a wave number which is not necessarily the highest one [28].

Growth rates are usually represented as a function of wave number in order to observe the Darrieus-Landau instability. In Fig. 2.12 the temporal growth rate is being represented as a non-dimensional quantity and plotted against the non-dimensional wave number; both are multiplied by the flame transit time τ_t and the flame thickness δ respectively. As predicted by Darrieus and Landau, the growth rate increases linearly with small wave numbers. However, at higher wave numbers the thermal-diffusive effects counteracts the hydrodynamic ones causing the growth rate to decrease again. Growth rate curves are shifted downwards due to the influence of gravity [26] which is more effective for flames with low burning velocities.

3 Literature review

3.1 System Response Analysis

In the previous chapter we have shown that the heat release fluctuation in relation to the velocity describes the *Flame Transfer Function*. This relation is useful during experimental and numerical identification of the *FTF* as there are given methods to control the input (acoustic modulations) and track the output.

However, in order to theoretically identify the *FTF*, this will require us to go a little further into physical detail. From basic thermodynamics. We know that instantaneous heat release is a function of the consumed mass flow and the heating value of the fuel or

$$\dot{Q} = \dot{m}_f H_u. \tag{3.1}$$

If we are to decompose the fuel mass flow $\dot{m}_f$, we find it to be a function of the flame propagation speed S, the flame surface area A, the mixture density ρ and the fuel content as a function of air excess ratio Λ and the stoichiometry factor K_s [12]. Eq. (3.1) could be written as

$$\dot{Q} = S \cdot A \cdot \rho \cdot \frac{1}{\Lambda} \cdot \frac{H_u}{K_s}. \tag{3.2}$$

According to Freitag [12], considering the small perturbations, Eq. (3.2) could be given in a linearized form as

$$\frac{\dot{Q}'}{\overline{\dot{Q}}} = \frac{S'}{\overline{S}} + \frac{A'}{\overline{A}} + \frac{\rho'}{\overline{\rho}} + \frac{\Lambda'}{\overline{\Lambda}}. \tag{3.3}$$

Assuming a constant air to fuel ratio for a perfectly homogeneous mixture we then have $\lambda' = 0$. For laminar flames, the flame propagation speed S (or S_L for laminar) is independent of velocity fluctuations and thus S'_L is also equal to zero. According to the authors of [5], a flow with a low Mach number has negligible density fluctuations ρ'. Equation Eq. (3.3) then could be reduced to

$$\frac{\dot{Q}'}{\overline{\dot{Q}}} = \frac{A'}{\overline{A}} \tag{3.4}$$

and finally the *FTF* could be represented in terms of area and velocity fluctuations

$$FTF = \frac{A'/\overline{A}}{u'/\overline{u}} \tag{3.5}$$

3.1.1 Proposed Analytical Models for the FTF

The fact that the variation in heat release is only controlled by that on the flame surface area is a good start for the theoretical analysis for the *FTF*. Schuller, Durox and Candel [27] for example made use of the relation in Eq. (3.5) together with instantaneous flame front position described in Sec. 2.3.3 to come up with a unified *FTF* model for laminar flames.

Conical Flames

They considered for conical flames the flame surface area to be calculated by integrating the instantaneous flame front position over the burner radius, the flame area fluctuations is then $dA' = 2\pi(R-x)dl$. Since that the flame shape fluctuation results affects the flame surface area, the first order estimate of the area fluctuation in terms of the flame position ξ is given by

$$A'(t) = \frac{2\pi}{\tan\alpha}\int_0^R (R-x)\frac{\partial\xi}{\partial x}dx. \tag{3.6}$$

We know by the Fourier transform that $\xi(X,t) = \tilde{\xi}(X)e^{-i\omega t}$ and therefore the area too $A'(t) = A'e^{-i\omega t}$. We also know that the flame displacement at steady state is equal to zero, or $\tilde{\xi}(0) = 0$ and therefore we get

$$A' = \frac{2\pi}{\tan\alpha}\int_0^R \tilde{\xi}dx. \tag{3.7}$$

In Sec. 2.3.3 we have introduced two approaches for modeling velocity modulations. Same were considered here for the determination of the *FTF*. Considering a *uniform velocity perturbation*, substituting Eq.(2.39) into Eq.(3.7), for FTF_{UCO} stands for a *Uniformly perturbed Conical Flame Transfer Function*, they got for Eq.(3.5) the expression

$$FTF_{UCO}(\omega_*) = \frac{2}{\omega_*^2}[1 - e^{i\omega_*} + i\omega_*]. \tag{3.8}$$

A similar analysis was made for *axial convective wave* model and a general expression for the *Convectively perturbed Conical Flame Transfer Function* was found to be

$$FTF_{CCO}(\omega_*,\alpha) = \frac{2}{\omega_*^2}\frac{1}{1-\cos^2\alpha}\Big[1 - e^{i\omega_*} + \frac{e^{i\omega_*\cos^2\alpha} - 1}{\cos^2\alpha}\Big]. \tag{3.9}$$

They came up then with three different expressions for three specific cases, they found that in the limit of large cone angles, where the flame approaches being normal to the flow, they get the same expression as the *uniform velocity perturbation* where it becomes only a function of the reduced frequency

$$\lim_{\alpha\to\pi/2} F_{CCO}(\omega_*,\alpha) = F_{UCO}(\omega_*). \tag{3.10}$$

As the angle decreases where the flame approaches being parallel to the flow the expression (3.9) becomes

$$\lim_{\alpha\to 0} F_{CCO}(\omega_*,\alpha) = \frac{2}{\omega_*^2}\big[(1 - i\omega_*)e^{i\omega_*} - 1\big]. \tag{3.11}$$

And in the case of long wavelength limit $(kR) \ll 1$, where the case is considered compact in comparison with the perturbation wavelength the transfer function becomes

$$\lim_{\omega_* \to 0} F_{CCO}(\omega_*, \alpha) = 1 + i(1 + \cos^2 \alpha)\frac{1}{3}\omega_* + O(\omega_*^2). \tag{3.12}$$

One of the weaknesses of the *axial convective wave* model is the violation of the continuity equation [2]. Cuquel, Durox and Schuller [2] have proposed another convective wave transfer function model for the conical flame that actually satisfies the mass balance. We denote the present model as FTF_{CCOC} which stands for *Flame Transfer Function with Continuity satisfaction*. This writes

$$FTF_{CCOC} = \frac{1}{i(k_* - \omega_*)} \cdot \left[2\left(1 - i\frac{1}{2}k_* - \frac{1}{2}\frac{k_*}{k_* - \omega_*}\right)\left(\frac{e^{ik_*} - 1}{ik_*} - \frac{e^{i\omega_*} - 1}{i\omega_*}\right) + \left(e^{ik_*} - \frac{e^{ik_*} - 1}{ik_*}\right)\right]. \tag{3.13}$$

where k_* and ω_* are both dimensionless flow wavenumbers, while the latter is related to flame front deformations propagating at speed $v_0 \cos\alpha$ along the flame front. For a flame front length L, flame height H and flame angle α, these numbers are given bu the expressions

$$\begin{aligned} k_* &= \frac{\omega}{v_0} H \\ \omega_* &= \frac{\omega}{v_0 \cos\alpha} L \end{aligned} \tag{3.14}$$

Results of the three models were compared and it was found that the gain of FTF_{CCOC} tends to be larger than the other models and is characterized by higher amplitude oscillations. However, its phase agrees with the model with uniform velocity modulation, FTF_{UCO}, at low frequencies and features the correct asymptotic behavior at higher frequencies that has been already predicted by the convective model FTF_{CCO} [2].

With regards to experimental validation in the low frequency range, FTF_{CCO} appeared to over-predict the experimental data while FTF_{UCO} does very well agree with it. The FTF_{CCOC} model however gives better results in that frequency range by satisfying the continuity.

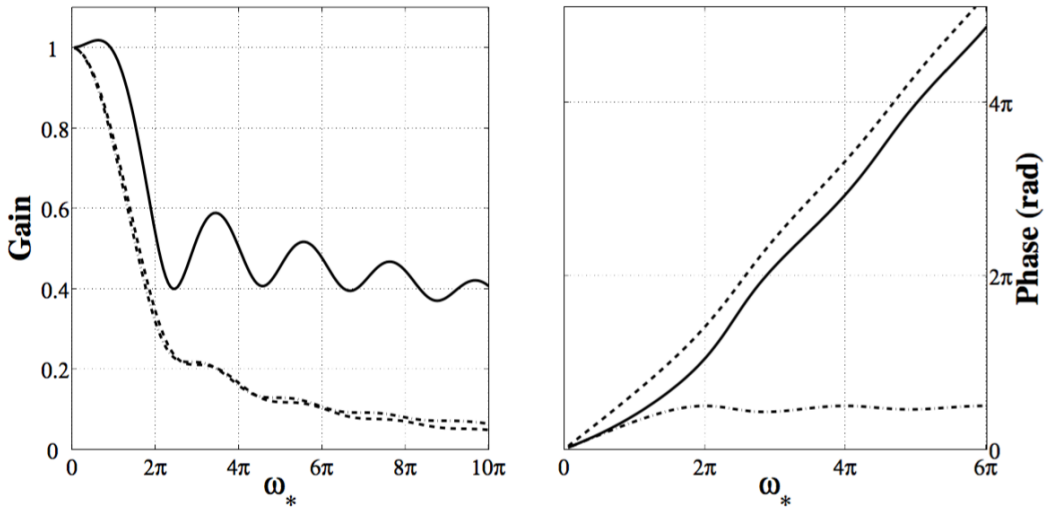

Figure 3.1: Gain and phase of the FTF the three models [2].Solid:FTF_{CCOC}. Dashed-dotted:FTF_{UCO}. Dashed:FTF_{CCO}

3.2 Flame Front Instability

3.2.1 Experimental Determination of Flame Growth

Truffaut and Searby [28] have attempted to measure the growth rate of the instability on an inclined flame over a wide range of wavenumbers and flame speeds. They used a laminar slot burner for the sake of producing an inverted V premixed flame. The perturbation to the flame was made via an electrostatic deflection system. To produce the laminar velocity profile at the exit, they fed a propane-air-oxygen mixture at the burner bottom . The burner included a divergent section, a settling chamber, a convergent section and a nozzle. The incoming flow was separated using glass beads that was inserted inside the divergent section. By means of an aluminium honeycomb, followed by three metal grids of decreasing mesh size inside the square settling chamber, the flow turned into laminar. The flow was accelerated via the 2D convergent section and fluctuations were reduced to a negligible value of the mean flow. Finally a 2D inverted V flame was provided at the exit. To avoid a strong thermal boundary layer, the convergent section and nozzle walls were water cooled at the fresh mixture temperature.

A thin tungsten rod was placed on one side of the flame in order to anchor it right at the exit see Fig. 3.2. An alternating high voltage is then applied to oscillate the tungsten rod and perturb the flame at the corresponding side. The resulting flame displacement produced sinusoidal 2D wrinkling that has a parallel axis to the burner slot at the flame front. Furthermore, A precise control of the initial amplitude and the frequency of the wrinkle was possible via the applied signal. The wrinkles were observed to be convected downstream by the gas flow and its amplitude was increasing exponentially. The laminar flame velocities (ranging from 0.43 m/s to 0.27 m/s) were controlled via the equivalence ratios which ranged from 1.05 to 1.33 for the propane-air flames. While for flames with 28% oxygen at equivalence ratios of 1.05 and

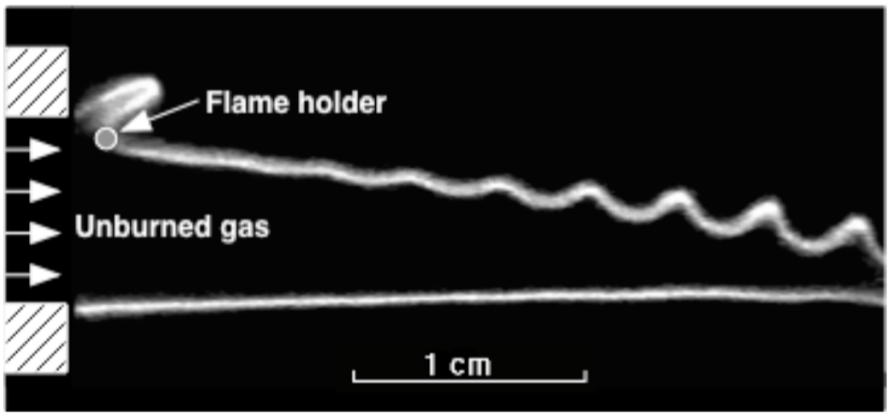

Figure 3.2: Growth of Darrieus-Landua instability of a propane-air-oxygen flame [26].

1.33, the velocities were 0.69 m/s and 0.51 m/s. The gas flow velocities were 7.4 m/s, 6.05 m/s and 8.56 m/s.

Using a short exposure intensified camera, they were able to capture several snapshots of the wrinkled flame. They used then these images to obtain the amplitude and the wavelength of the wrinkles as a function of the distance from the flame holder. After low pass filtering of the curve the maxima and minima were located, interpolated, and the peak to peak amplitude was calculated as in Fig. 3.3.

In order to calculate the growth rate they considered the evolution of the peak to peak amplitude of the flame front. They first ignored the initial points due to the electric field vibrated rod. They also ignored the downstream region where saturation starts to appear due to formation of cusps. To the rest of the points, where the exponential growth is observed (shown by the linear blue line on the semi-log plot in Fig. 3.4), they fitted an exponential function in order to calculate a good estimate for the spatial growth rate σ_x. They converted the spatial growth rate into the temporal growth rate σ via multiplication by the convection velocity u_c.

The non-dimensional growth rate $\sigma\tau_t$ was then plotted against the non-dimensional wave number $k\delta$ and compared to the theoretical dispersion relation described by Clavin and Garcia [8] in Eq. (2.44) where the gravitational acceleration set to zero. The Markstein number was tuned to the best fit of the measured results for each flame; Fig. 3.5

Observations and results

It has been observed by [28] that the wrinkles are propagating downstream with the a constant velocity equal the convected tangential component of the inflow velocity along the flame front. Also the wrinkles amplitude was seen to grow exponentially up to the saturation point where cusps start to form. They also found that the dimensional growth rate is typically between $150s^{-1}$ and $300s^{-1}$. It can also be seen from Fig. 3.5 that the growth rate decreases again at very high wavenumbers, this is due to the combined effects of hydrodynamics and preferential diffusion.

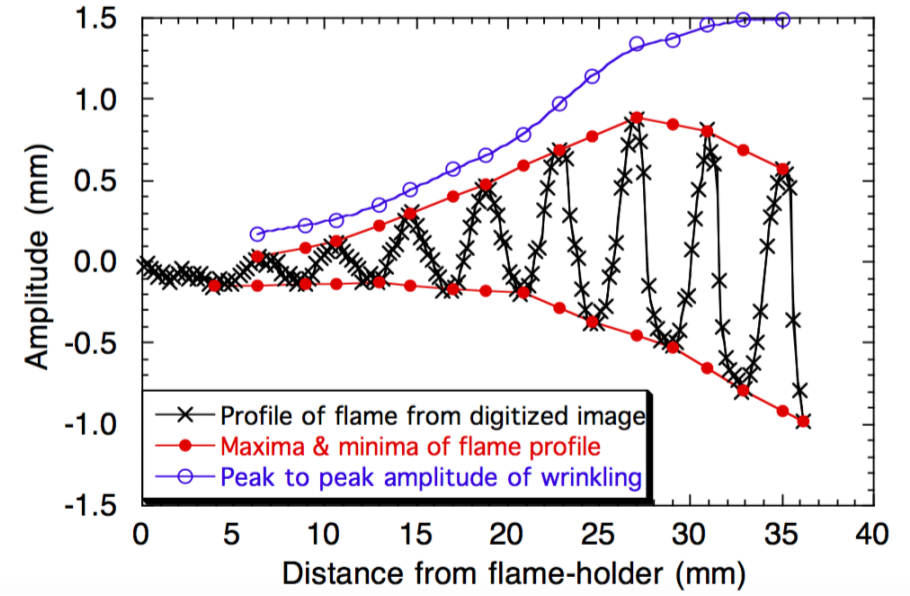

Figure 3.3: Flame profile of wrinkling amplitude [26].

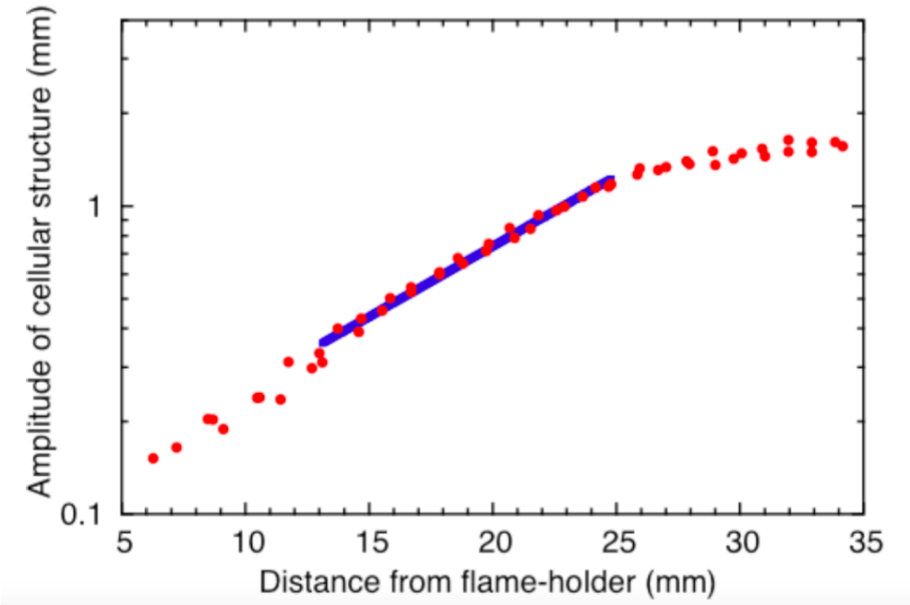

Figure 3.4: Semi-log profile of peak to peak wrinkling amplitude [26].

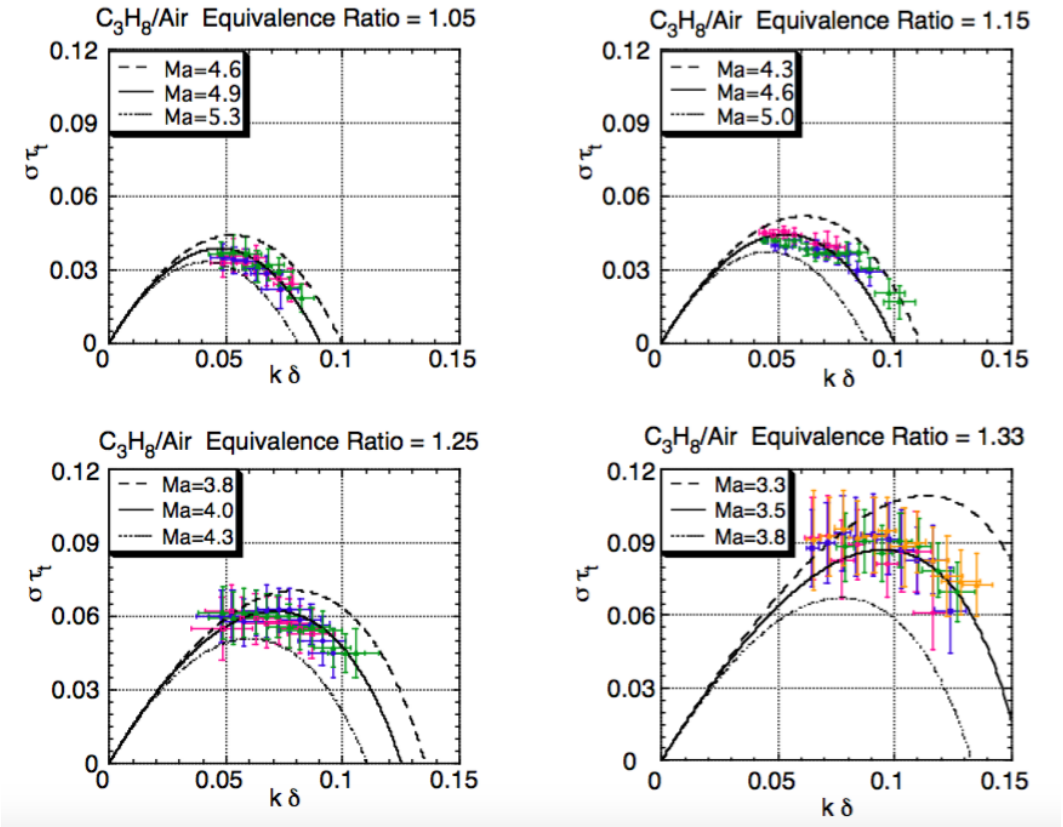

Figure 3.5: Measured growth rate of Darrieus-Landau instability as a function of imposed wavenumber. Curves are calculated using the dispersion relation for the growth rate [26].

4 Numerical Setup

In this thesis *OpenFOAM* is used for CFD simulation and *Paraview* is used for visualizing the results. Cases are constructed and submitted to the *Leibniz-Rechenzentrum (LRZ)* for parallel computation. Afterwards *Matlab* is used for post-processing purposes. In this case flame laminar speed is very small such that the Mach number (S_L/c) is much less than one. The flow is therefore considered incompressible. However the density can change due to temperature variation. The solver used here is the same one used by Jaensch et al. [23].

4.1 Case setup

4.1.1 Geometry

A common approach in CFD applications is, whenever possible, to reduce the case geometry from a three-dimensional (3D) case into a two-dimensional (2D) one. This has the huge advantage of reducing the computational cost. The only cases where this approach is applicable and results in 2D simulations having the same results as 3D simulations is when the case is actually symmetric. A very known example is the fluid flow in a straight pipe where the geometry can be reduced to 2D due to the fact that the case is axis-symmetric.

In a similar way is our case, the one shown in Fig. 4.1. In this case we reduced the 3D geometry of a conical shaped flame into 2D, using the fact that the flame is axis-symmetric in the axial flow direction. It is for this reason that even the 3D preview in the figure looks like a slit case. However, the geometry is created such that if it's rotated around the lower axis in the flow direction, it will give us a cylindrical geometry. For this to be considered during the computations, a special boundary condition has to be applied, it is called a *symmetrical* boundary condition. It basically sets the values of the flow fields just adjacent to the solution domain as the values at the nearest cells inside the domain.

Fig. 4.2 shows us the flame profile of premixed lean mixture of air and natural gas after reaching a steady state. This is the starting point of our numerical simulations. In this figure, the thin layer separating the fresh mixture (red) and the burnt gases (blue) is considered the flame front, where most of the physical and chemical properties changes take place. Since that the flame front is the most interesting zone for our analysis, it is necessary to avoid numerical errors in this zone as much as possible.

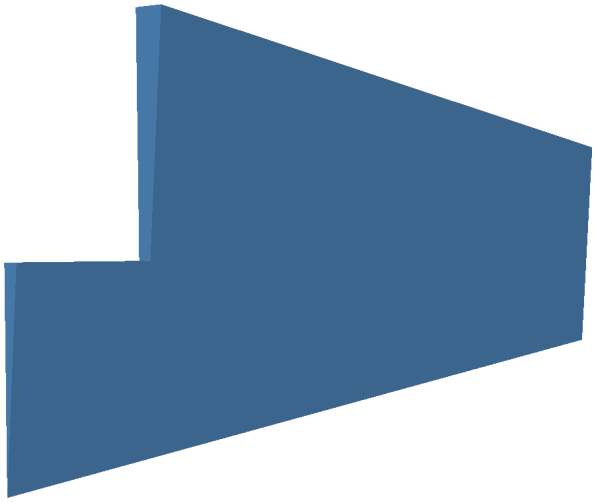

Figure 4.1: 3D surface view of the conical flame case.

Numerical accuracy in CFD is related to the flame resolution; the finer the mesh the more accurate the computations are as long as the mesh quality is maintained good (no skew faces, no high aspect rations between adjacent cells...etc.). Meanwhile, a too fine mesh implies that a higher computational cost is required. This is due to more than a reason, one of which is that with a finer mesh we are necessarily increasing the number of cells, eventually the time required for calculations per time step is also increased. Another reason is due to the limitation of the *Courant number*, which forces us to choose a small enough time step in order for the solution to converge and produce accurate results. Since that a smaller time step means more iterations are required per a certain period of simulation time, this is a determining factor in the computational time required.

It is for all of the above mentioned reasons, the mesh resolution shown in Fig. 4.3 was a good compromise between a fine mesh at our zone of interest (the flame front and it's adjacent layers) for fairly accurate calculations and a coarser mesh in the surroundings, where there is not a lot of physical and chemical changes happening, for reduced computational time.

Figure 4.2: Methane profile showing the flame front separating fresh and burnt gas sides.

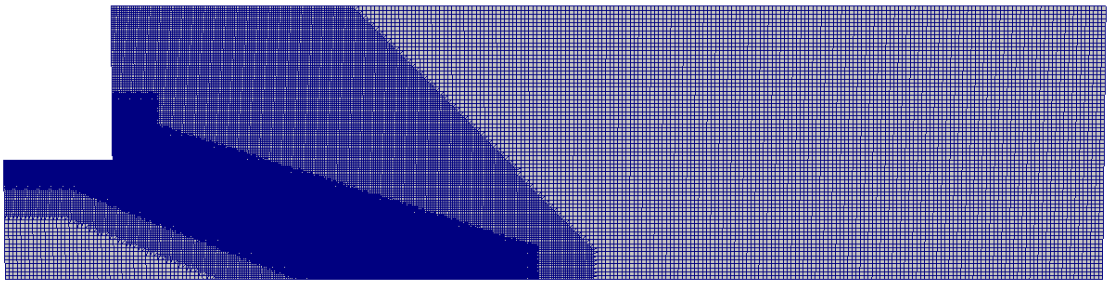

Figure 4.3: Mesh being refined at the flame front.

4.1.2 Boundary conditions

Before discussing the fields boundary conditions let us first define the names given to the mesh regions. Besides the $axis$ of symmetry, there are six more patches that describes the mesh of our case, starting with the duct $inlet$, where the mixture of air and methane comes from, at the west side of the geometry shown in Fig. 4.2. The radial duct wall, $wall_{duct,rad}$, is what prescribes the passage of the fresh gases before starting to diffuse in the chamber. The chamber wall boundaries consist of the one which is normal to the duct radial wall, in this context we call it $wall_{ch}$, and the radial chamber wall, $wall_{ch,rad}$, at the north side of our geometry. We then have the $outlet$ at the east side which allows the exit of the burnt gases after the combustion process. Finally, the front and back sides of our geometry are the symmetrical boundaries that allows the use of 2D simulation, we call them $wall_{sym}$.

Boundary	$U_{inlet}\,[ms^{-1}]$	$T\,[k]$	$p\,[pa]$	$Spicies$
$inlet$	$\overline{U}(U'A+1)$	fixedValue	zeroGradient	fixedValue
$outlet$	zeroGradient	zeroGradient	fixedValue	zeroGradient
$wall_{ch}$	fixedValue (0)	$\overline{T}(T'A+1)$	zeroGradient	zeroGradient
$wall_{ch,rad}$	fixedValue (0)	Heat flux	zeroGradient	zeroGradient
$wall_{duct,rad}$	fixedValue (0)	zeroGradient	zeroGradient	zeroGradient
$wall_{sym}$	wedge	wedge	wedge	wedge
$axis$	empty	empty	empty	empty

Table 4.1: Boundary types of physical properties.

Table 4.1 summarizes the boundary conditions applied to the physical fields. At the $axis$ no computations are supposed to be done and in theory there are no fields, the boundary $empty$ is therefore applied to all the fields. The $wedge$ boundary condition is the one that is used in *OpenFOAM* for axis-symmetric cases to define a symmetry wall, it is used in our case at the front and back symmetry walls for all of the fields. A $fixedGradient$ boundary condition applies the *Neumann* condition, sets the derivative to a specific value. When this value is zero, we can make use of the boundary condition $zeroGradient$ instead. Meanwhile, the value-specified, *Dirichlet*, boundary condition is represented in *OpenFOAM* by the $fixedValue$. The $groovyBC$ is a powerful tool that allows us to create a time varying boundary for a specific field; this is very useful in our case in order to be able to excite the steady state simulation with different harmonics and/or impulses as will be explained later in this subsection.

Because the velocity and pressure are usually coupled by the *Navier-Stokes* equations, it might result in wrong calculations to set them both to defined values at the same location. For this reason, a common approach in CFD problems is whenever defining the value of either at a certain boundary to keep the other one floating, setting its derivative to zero is a fairly good solution. In our case, we set the velocity to zero at the walls considering the *no-slip* condition. Meanwhile the pressure gradient has been set to zero. It was again set to zero at the inlet where the velocity was defined using the $groovyBC$. At the $outlet$ the p was set to the atmospheric pressure with the derivative of U_{inlet} equal to zero.

The incoming fresh gas from the $inlet$ was considered to have a fixed temperature of $300k$ (room temperature). The radial wall duct was assumed to be an adiabatic wall so that T doesn't change and therefore $zeroGradient$. Similarly at the $outlet$ where burnt gases exit the combustor while maintaining the same temperature. For flame base excitation purposes another function was implemented for the temperature at the radial wall chamber.

Flame excitation

In this work, we decided to use two ways to excite the steady state flame. The first approach considers adding another velocity term to the inlet. The velocity function at the inlet then

writes

$$U_{in} = \overline{U}(U'A+1)(1i+0j+0k) \tag{4.1}$$

where $\overline{U}$ is the starting value that was used to reach the steady state solution, U' is an input time variable array of velocities, A is its amplitude and the vector $(1i+0j+0k)$ means that U_{inlet} is only in the axial direction. In case of harmonic excitation, the time varying array U' is a *Matlab* generated sinusoidal function of time with unity amplitude and frequency f.

The second method of excitation is via oscillating the flame base which is anchored to the radial wall of the chamber. This is done through changing the temperature of $wall_{ch,rad}$ according to the function

$$T_{wall} = \overline{T}(T'A+1) \tag{4.2}$$

where again $\overline{T}$ is the temperature meant to be at the steady state, A is the desired amplitude and T' is a time varying array created the same way as U'.

4.2 Post processing

With making use of the fact that the flame front, separating fresh from burnt gases, can be considered as an isotherm (has a constant temperature), we have been able to filter out its points using the *contour* filter in *paraview* in order to extract all the points with T equal to 1200 k. The points were then imported to *Matlab* and some functions were created for the sake of analyzing the flame front behavior.

Firstly, the points were filtered out from repeated values and interpolated along a common grid. Fig. 4.4 is an example of the flame front after being imported into *Matlab* for post processing. Here the blue line shows the flame front position at steady state while the red line is the flame front after being excited by 120 Hz at the flame base temperature

Normal-to-flow oscillations of the flame between each snapshot and the steady state flame have been calculated. Then a function has been created to filter out all the $maxima$ and $minima$ of the different snapshots and bring them together into a double array. This is shown in Fig. 4.5 where the blue line describes the amplitude of the oscillations while maxima and minima of the flame front are emphasized by the small crosses and circles.

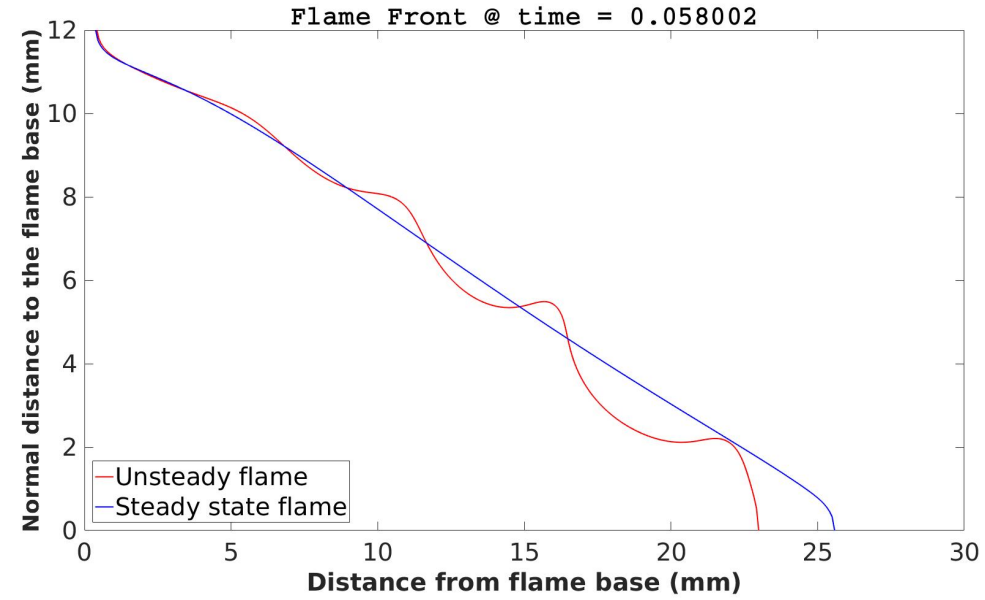

Figure 4.4: Flame front instability excited at 120 Hz by temperature at the flame anchor.

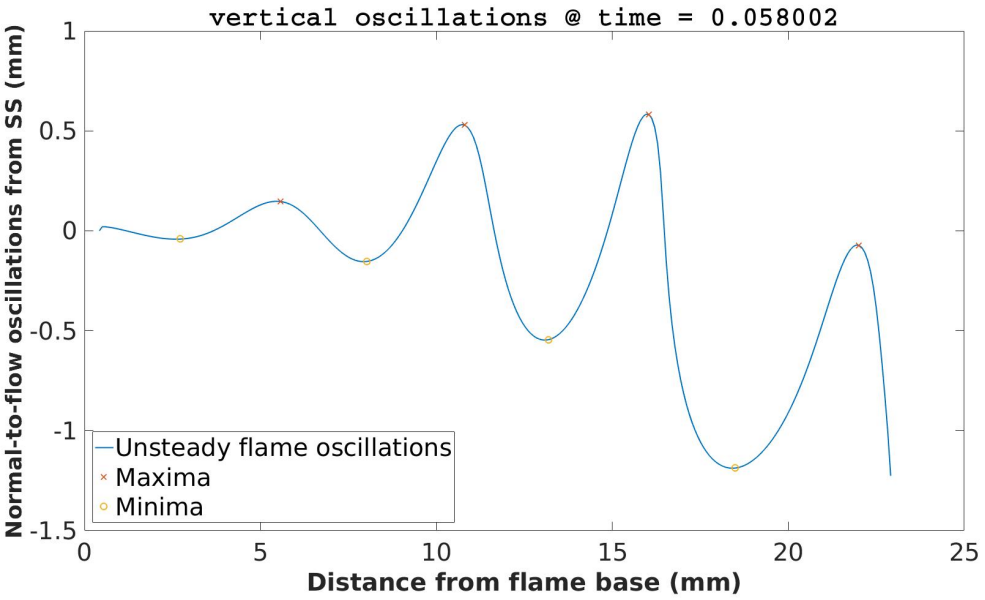

Figure 4.5: Maxima and minima of the flame front excited at $120 Hz$ by temperature at the flame anchor.

5 Results

5.1 Velocity vs Temperature Excitation

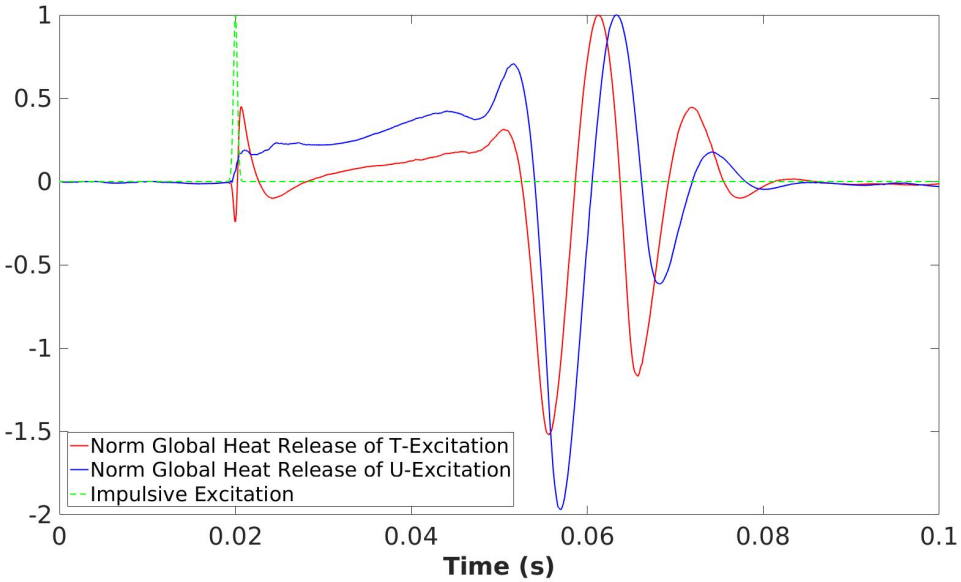

Figure 5.1: Comparison of the global heat release response to impulsive excitation of inlet velocity and flame base temperature.

In the following analysis, we are focusing on the flame instability as being subjected to different excitation methods. You may have noticed in the previous chapter that we have considered two approaches to excite the flame, inlet velocity modulation and flames base temperature modulation. This came out of our interest in the flame behavior in response to both methods, and how similar it might be. Nevertheless we have noticed from our results that regardless the actual way of excitation, the results are actually very comparable.

Fig. 5.1 shows the normalized heat release in response to impulsive excitation. First of all, we have to keep in mind that comparing the amplitudes does not tell us anything. We know that the physics of both approaches are different and just by trial and error we succeeded to have relatively comparable amplitudes for the heat release. However, for a linear system we are mostly interested in the qualitative response of that system.

Qualitatively speaking, it has been seen that by the exact time of the impulsive excitation 0.02 s there has been an immediate influence on the heat release which has been followed

by gradual increase. At 0.05 s the major effect of the impulse started to appear in the heat release as three consequent overshoots with the highest one in amplitude being the middle one happening shortly after 0.06 s.

Further analysis including a comparison between both excitation ways, but in terms of the flame front behavior is included is sections 5.4.2 and 5.5 .

5.2 Response analysis

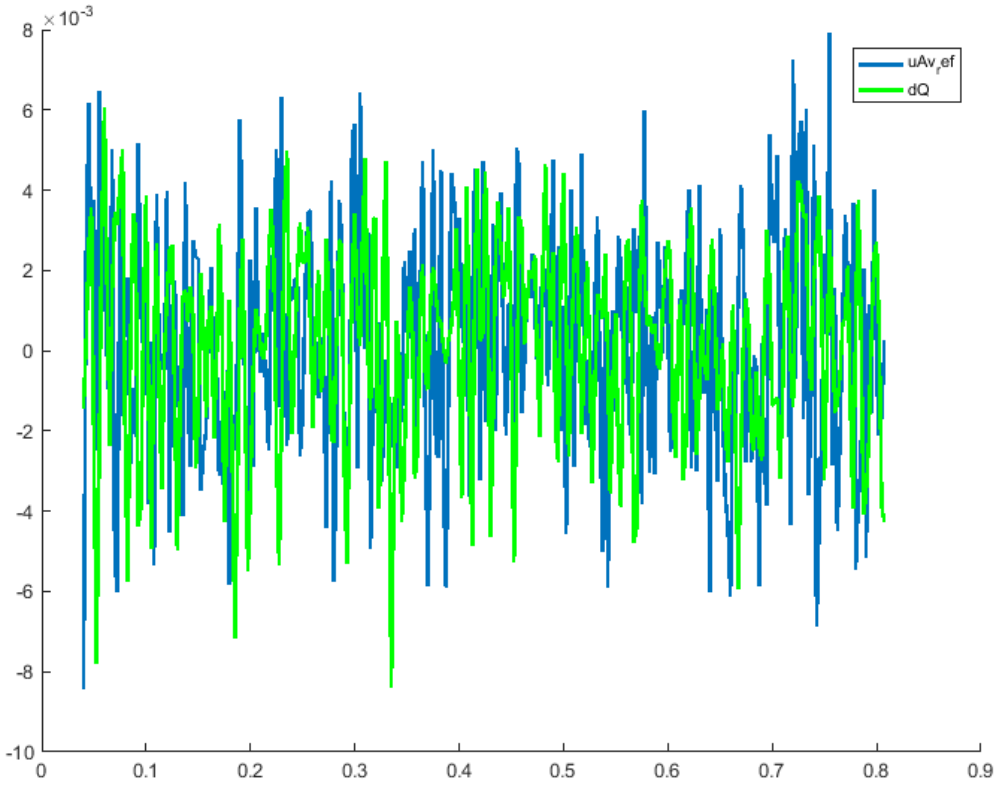

Figure 5.2: Broadband input and output signals. Input and output signals are represented in velocity modulation (blue) and the resulting global heat oscillation (green).

As mentioned before, the *FTF* relates the velocity perturbations to heat release perturbations. However, determining the *FTF* using several different harmonic signals is very unpractical, since the simulation must be run for each forcing frequency. One alternative method is by using multi-tone signals to excite the flame [9]. This enables us to modulate the flame over a wide range of frequencies and obtain its *FTF* just at once. In this thesis a *Matlab* tool is used to obtain a broadband signal which has been used as an input signal for the velocity excitation (U' in Eq.(4.1)). The inlet (velocity) and the output (heat release) signals are shown in Fig. 5.2.

Transfer function

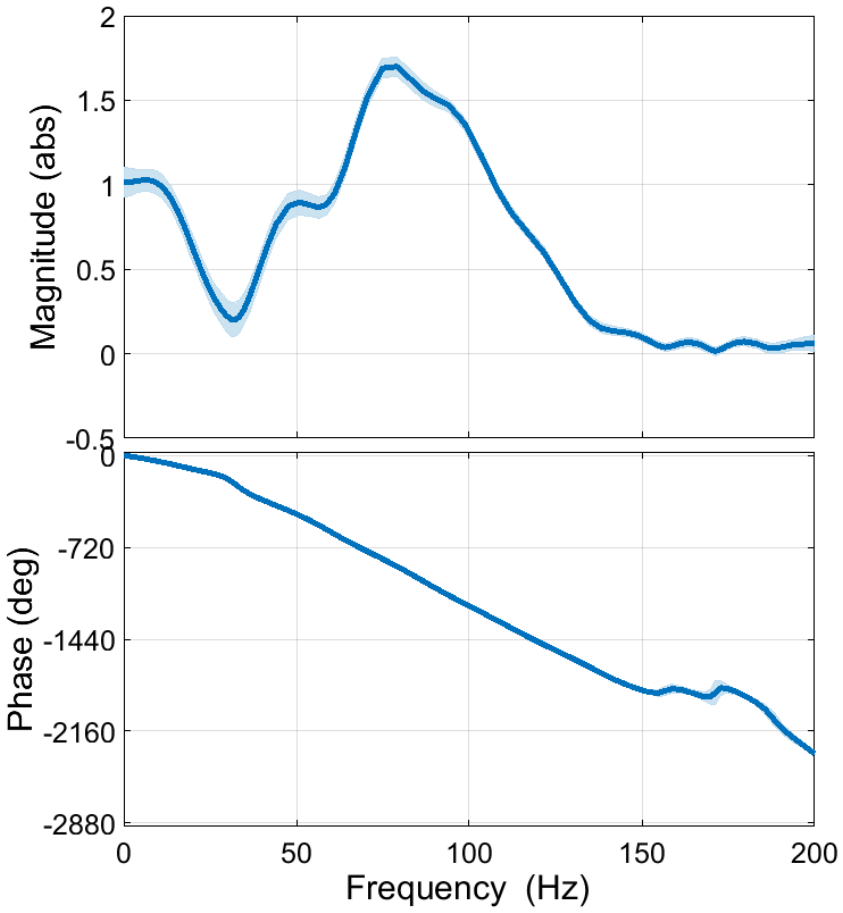

Figure 5.3: Gain and phase of FTF

Fig. 5.3 shows results for the gain (upper) and phase lag (lower) of the *FTF*. A gain of unity is obtained at very low frequencies. It then decreases and reaches a minimum of around 0.2 at about 30 Hz. The gain increases again to reach values higher than unity for frequencies more than 60 Hz to reach a peak value of 1.7 at about 80 Hz. A small bump could be noted at about 50 Hz though. The flame then starts to act as a low frequency filter in response to higher frequencies, causing the gain to progressively decrease. It reaches again lower than unity at 110 Hz and the cutoff frequency (where the gain falls below 0.5) is 125 Hz.

The *FTF* phase lag starts from zero and decreases constantly with higher frequencies. An inflection point could be seen at the frequency where the gain reached the minimum magnitude (30 Hz). The gradient then becomes constant after 30 Hz and up to higher frequencies. A qualitatively similar response has been found experimentally as well as numerically by Blan-

chard et el [17] when they tested an M-shaped laminar premixed methane-air flame.

5.3 Flame Front Growth Rates

In this section we are trying to analyze the instability of the flame front when it is being subjected to different methods of excitation. We are mainly interested to observe the effect of the Darrieus-Landau instability in order to find a the relation with the flames stability analysis.

5.3.1 Harmonic Excitation

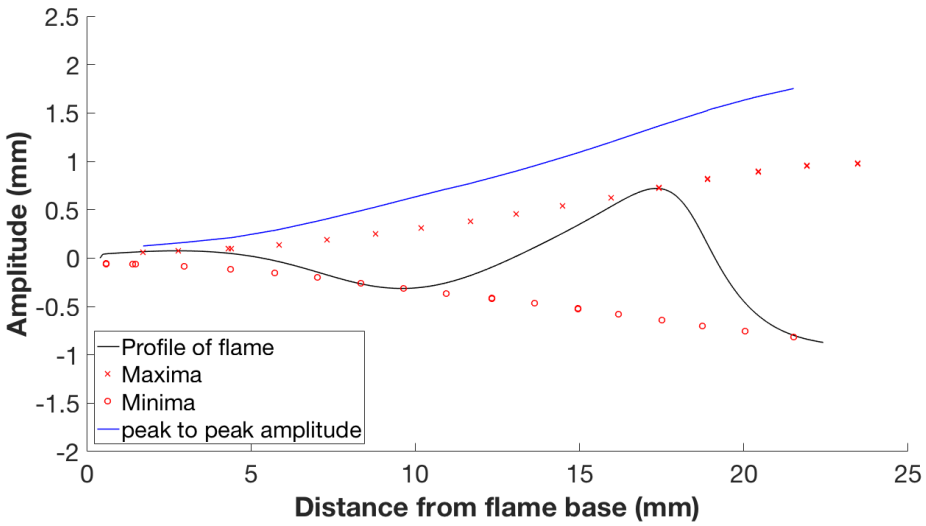

Figure 5.4: Flame profile of wrinkling amplitude excited by 50 Hz at the flame base temperature.

In this section excitation was made at different harmonic frequencies. The flame is observed and the Darrieus-Landau instability is calculated from the numerical results. The analytical dispersion relation explained in Chapter 2 is then used for our flame properties in order to compare the results with the numerical results.

Figures 5.4, 5.5 and 5.6 show the flame profile when it is exposed to the harmonic frequencies 50, 80 and 120 Hz respectively. In these figures the solid black lines represent the flame profiles at a certain snapshot from the numerical simulation. The small red crosses and circles stand for the maxima and minima taken from all of the snapshots till the end of our simulation.

Finally the solid blue line represent peak to peak amplitude, addition of maxima and minima per point location after being interpolated. The latter is used to find the growth rates.

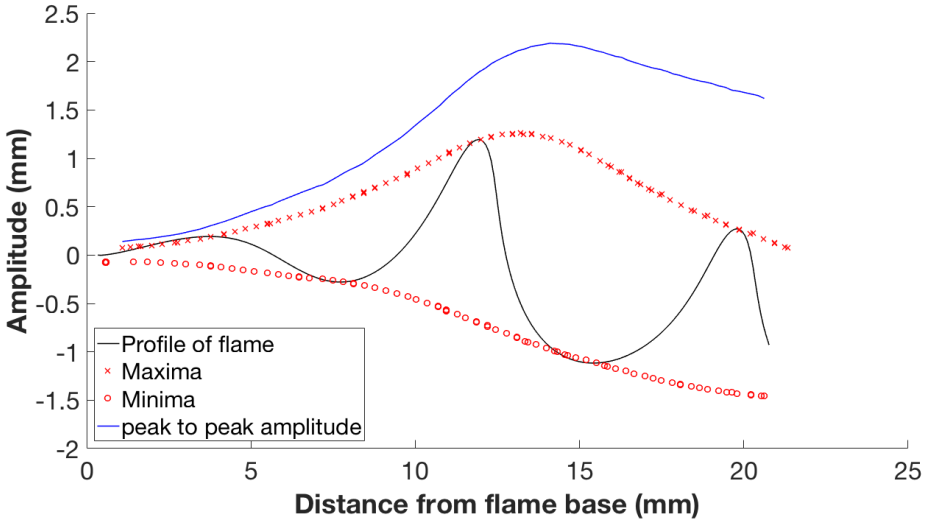

Figure 5.5: Flame profile of wrinkling amplitude excited by 80 Hz at the flame base temperature.

At 50 Hz the flame appeared to grow equidistantly towards both the fresh and the burnt gas sides. For this flame, the peak to peak growth has shown a linear behavior with no saturation at the end. At 80 Hz the flame has grown exponentially in both sides with the formation of sharper cusps towards the downstream gases than the upstream. Eventually the peak to peak growth has been observed to grow exponentially. However, it reached its peak value at a distance of 14 mm from the flame base.

A flame excited at 120 Hz has the closest behavior to the one experimentally tested by Truffaut and Searby [28]. The sharpness of the cusps downstream is not much sharper than that upstream as it was noticed at 80 Hz. Moreover, the peak to peak amplitude ended by a saturation phase with no maximum point being in the middle of the flame.

On a semi-log plot, the peak to peak amplitudes from the three results are plotted together as in Fig. 5.8 in order to observe the exponential growth. Even though the growth at 50 Hz was not observed to be exponential, the linearity limit from the semi-log plot is estimated to be after 12 mm away from the flame base. By considering only this part of the flame, we were able to derive an exponential function for each flame using the least square regression method. The data are plotted together in Fig. 5.9 and the highest growth rate appeared to be happening at 80 Hz

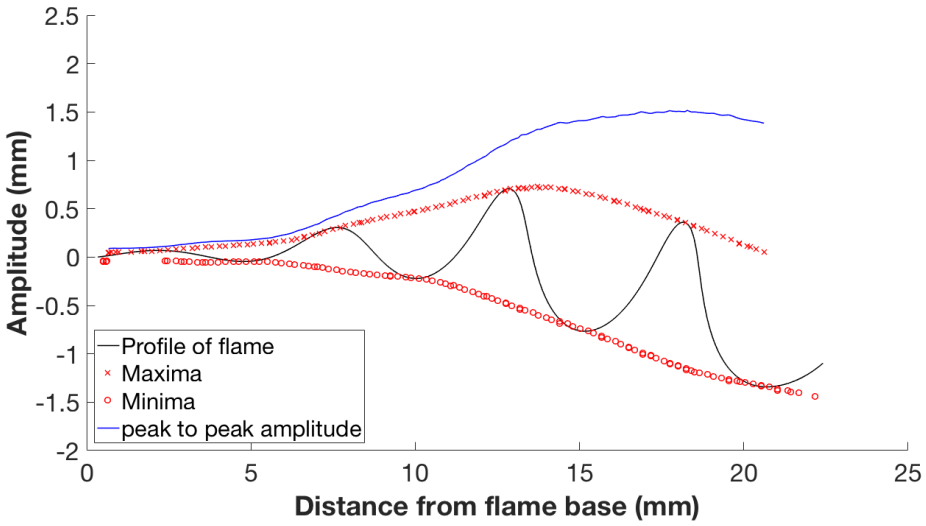

Figure 5.6: Flame profile of wrinkling amplitude excited by 120 Hz at the flame base temperature.

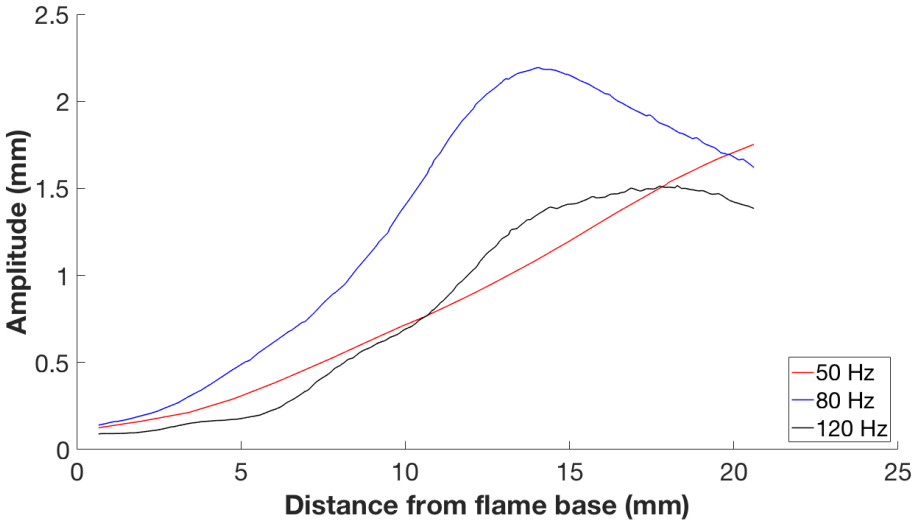

Figure 5.7: Comparison of peak to peak spatial flame growth between 50, 80 & 120 Hz.

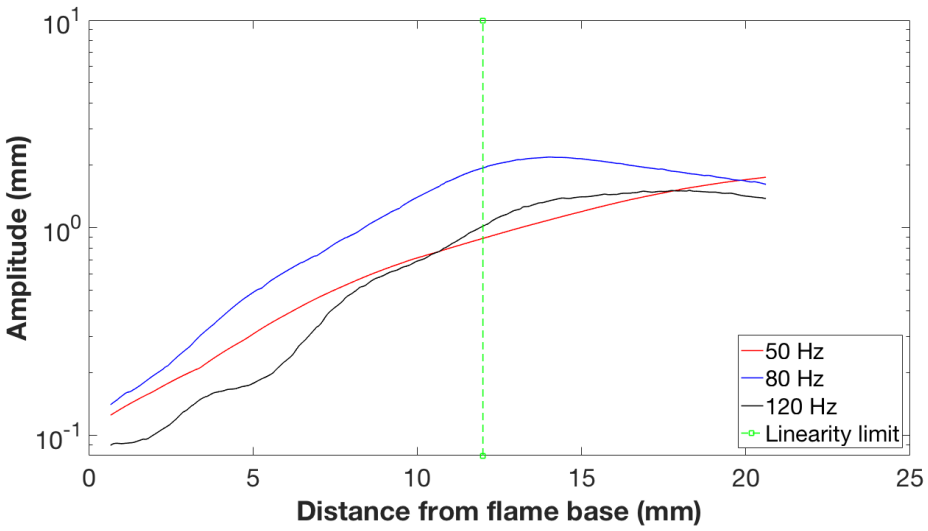

Figure 5.8: Semi-log plot comparison of the data from Fig. 5.7 .

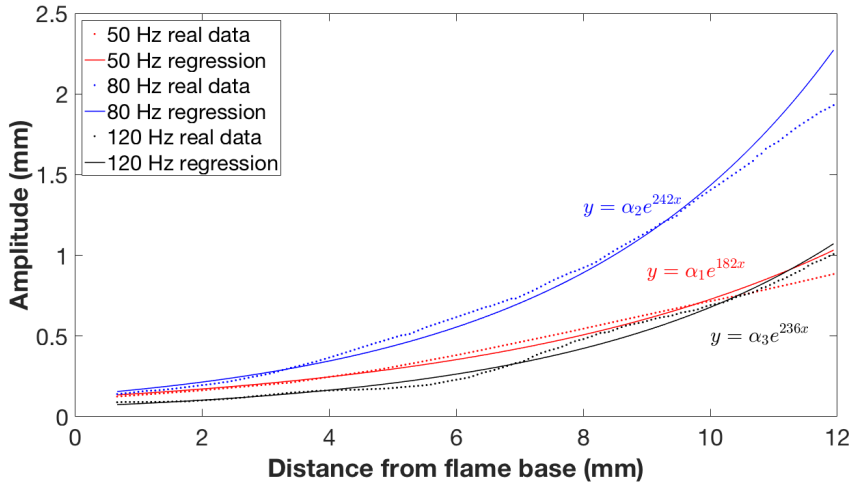

Figure 5.9: Linear regression on of the data from Fig. 5.7 .

Now that we already have information about the spatial growth rate, we would like to find the temporal one. This could be done by multiplying the spatial growth rate by the convection velocity as done by [28]. Considering that we know flame axial length and the flame base height, a flame angle could be roughly estimated. This flame angle is useful to estimate the inlet gas velocity component along the flame front, which is assumed to be the same as the convection velocity of the wrinkles. First we define the flame angle and the convection velocity as

$$\alpha = \tan^{-1} \frac{H_f}{L_f} \tag{5.1}$$

$$u_c = u_{\text{inlet}} \cos \alpha \tag{5.2}$$

where H_f and L_f are the flame's thickness and axial length, respectively. We then calculate the corresponding temporal growth rate as

$$\sigma_t = \sigma_x u_c \tag{5.3}$$

whereas σ_x is the spatial growth rate given by the exponent coefficients of the functions shown in Fig. 5.9. Table 5.1 summarizes the spatial and temporal growth rates of different harmonics.

	$\sigma_x\,[mm^{-1}]$	$\sigma_t\,[ms^{-1}]$
30 Hz	0.122	0.105
50 Hz	0.182	0.157
80 Hz	0.242	0.208
120 Hz	0.236	0.203
300 Hz	-0.300	-0.258

Table 5.1: Spatial and temporal growth rates for different harmonics.

From the Table 5.1 we noticed that the maximum growth rate appeared to happen at around 80 Hz. We have expected this due to the high instability that was seen in Fig. 5.4.

Comparison to theoretical methods

In order to fairly compare the flame response to the excited frequency, it was necessary to consider the effect of the flame thickness. The plot in Fig. 5.10 is therefore a plot of the reduced growth rate $\sigma\tau$ against the reduced wave number kδ where the parameters σ, τ and δ are explained in chapter 2 and the wave number k is given by

$$k = \frac{2\pi f}{u_c} \tag{5.4}$$

A derivation from the Landau model (2.42) that includes the curvature effect and therefore considers the effect of the Markstein number in the flame growth was found in [7]. It writes:

$$\sigma = k \cdot S_L \frac{E}{E+1} \cdot \left(-Mak - 1 \pm \sqrt{(Mak - E)^2 - (1 + 1/E)(E-1)^2} \right) \tag{5.5}$$

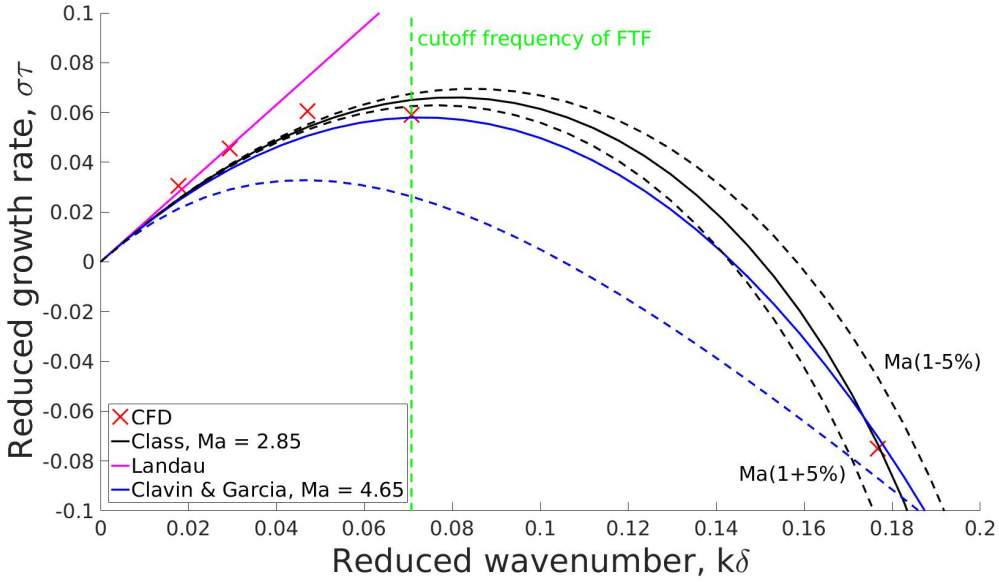

Figure 5.10: Flame profile disturbed with two wrinkles after temperature excitation.

The black solid line in Fig. 5.10 shows the prediction of the Darrieus–Landau instability according to this model. Note that Markstein number Ma was tuned to the best fit of the CFD prediction (red crosses). The effect of a +5% and −5% of this tuned Ma is represented by the dashed lines below and above the solid line respectively. Moreover, the simple linear model by Landau is represented by the magenta solid line.

The dispersion relation that was given by Clavin and Garcia [8] and represented by Eq. (2.44) predicted the behavior of the blue dashed line using for the same Ma (The method of how the flame parameters are calculated are given below). However using the same Ma and following the set of equations described in chapter 2, specially the integrals H and J described by Eq. (2.47) or alternatively Eq. (5.8), we were not satisfied with the prediction of this model. We therefore decided to use the parameters given by the closest case we found in the paper by Searby [26] and fit a new Ma to it, this is represented by the blue solid line. For this case, $J = 3.87$ and $H = 1.067$.

Calculation of the flame parameters

We know from our boundary conditions and the results of the simulation that the fresh gas temperature T_u is 300 k and the burnt gas temperature T_b is 2100 k. The flame thickness and transit time are calculated using Eq. (2.45) with the flame speed S_L calculated according to [16].

$$S_L = A\phi^B e^{-C(\phi-D)^2} \tag{5.6}$$

where ϕ is the equivalence ratio while A, B, C and D are constants that depend on the mixture composition, not to be confused with the constants defined for the dispersion relation (2.44).

The thermal diffusivity D_{th} is calculated according to Chapman-Enskog equation [1]

$$D_{th} = \frac{0.00266 T^{3/2}}{M_{AB}^{1/2} \sigma_{AB}^2 \Omega_D} \tag{5.7}$$

with M_{AB} being the molar mass of the composition, σ_{AB} and Ω_{AB} are temperature dependent coefficients. With the expansion ratio E given according to Eq. (2.43) and θ and $h(\theta)$ according to Eq. (2.48), the integrals H and J in Eq. (2.47) could be reevaluated in terms of temperature T as

$$\begin{aligned} H &= \int_{T_u}^{T_b} \big(h_b - h(\theta)\big) \cdot \frac{1}{T_b - T_u} dT \\ J &= (E-1) \int_{T_u}^{T_b} \frac{h(\theta)}{1 + (E-1)\theta} \cdot \frac{1}{T_b - T_u} dT \end{aligned} \tag{5.8}$$

The numerical values of the flame parameters are represented in Table 5.2 in $SI - units$

Flame parameter	Value
u_{inlet}	0.9015
α	0.3
ϕ	0.8
T_u	300
T_b	2100
S_L	0.2782
D_{th}	2.2481×10^{-5}
E	7
ρ_u	1.12
δ	8.0812×10^{-5}
τ_t	2.9049×10^{-4}
h_b	9.6880×10^{-5}
H	3.91×10^{-4}
J	-1.99×10^{-4}

Table 5.2: Spatial and temporal growth rates for different harmonics.

5.3.2 Impulsive Excitation

In order to get a better understanding of the flame dynamics, it was important to separate the effects of subsequent harmonic pulses and start to analyze the flame response as it is being subjected to one impulse. This impulse response test was run for the conical flame case with Re = 1240 and confinement ratio of 0.44.

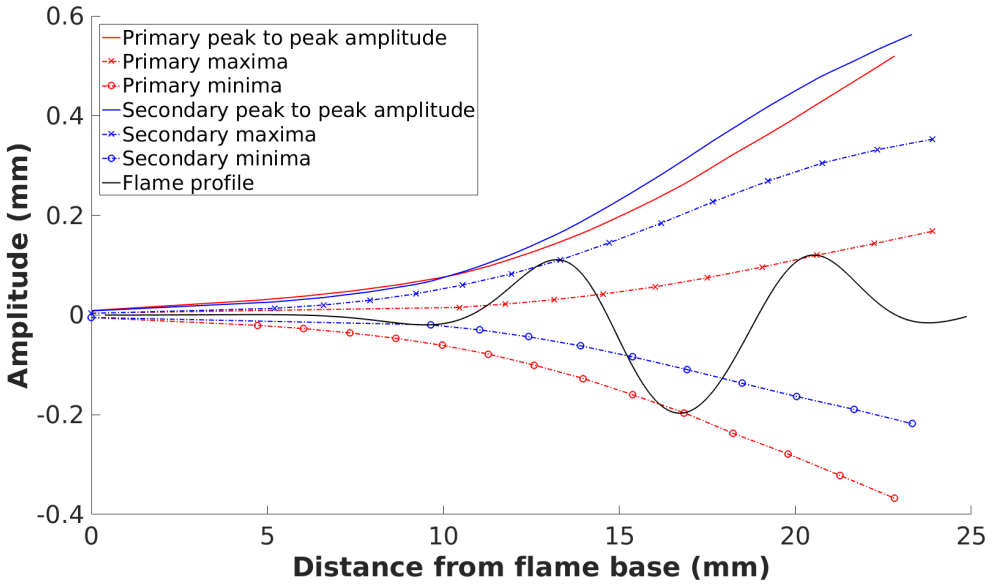

Figure 5.11: Flame profile disturbed with two wrinkles after temperature excitation.

In this context, two different methods of excitations are proposed: first method by exciting the velocity inlet by an amplitude of 3% of the mean inlet velocity. The second one however considers exciting the temperature at the flame base by an amplitude of 30% of the mean temperature at the flame base. The magnitudes of the different excitations have been chosen such that both approaches would have a quasi-similar amplitude of growth.

The flame front appearing in Fig. 5.11 was taken at 0.046 s. However, by considering all of the saved snapshots from start till the end of simulation, we could see how the flame actually grows in time as seen in Fig. 5.12. Considering that this is an impulse response test, we would have expected to see one wrinkle along the flame front that propagates until the flame tip. However, if you have a look at Fig. 5.11, you may notice the flame front (the black solid line) has two wrinkles, this is a surprising observation for us. A Matlab function is created to separate the two wrinkles of the flame front in order to observe the pattern of each, we call the first one primary wrinkle while we refer to the second one as a secondary wrinkle.

Fig. 5.11 shows us that when the flame is excited by the temperature impulse at its base, the first wrinkle had the tendency to grow faster towards the fresh gas side than the burnt side. On the contrary to the secondary wrinkle which grows more towards the burnt gas side. The peak to peak amplitudes, represented in the solid lines, are again calculated here for each wrinkle separately in order to estimate the Darreius-Landau instability. Using the linear regression to derive an exponential model for both wrinkles, the spatial growth rate is calculated. Equations (5.1) - (5.3) are then used to calculate the temporal growth rate. The results are shown in table 5.3.

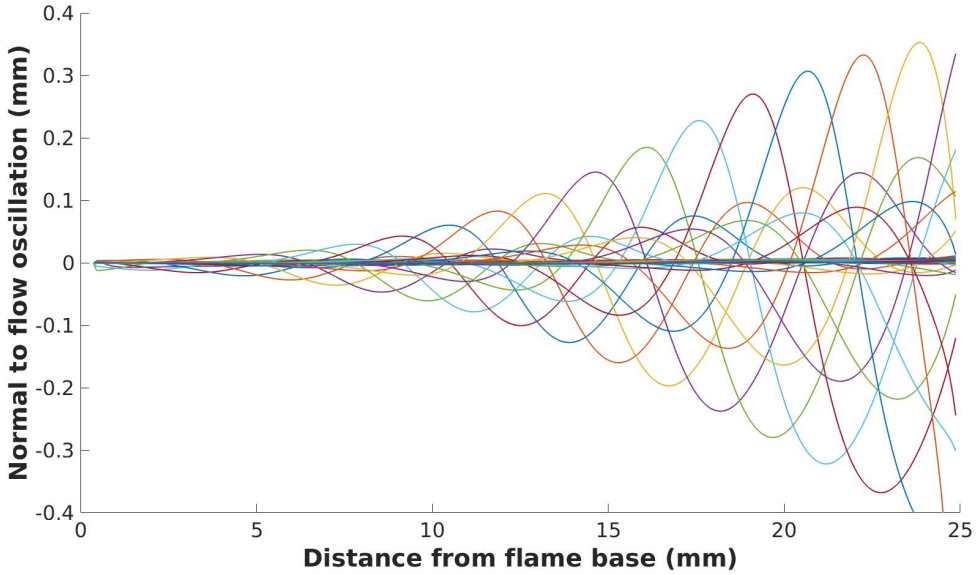

Figure 5.12: Flame front disturbance from time 0 s to 0.1 s after temperature excitation.

	$\sigma_x\,[mm^{-1}]$	$\sigma_t\,[ms^{-1}]$
Primary	0.174	0.149
Secondary	0.189	0.163

Table 5.3: Spatial and temporal growth rates of IR.

From table 5.3 it could be seen that the growth rates of both primary and secondary wrinkles resulting from the impulsive excitation are very comparable to that of the harmonic excitation represented by the data in table 5.1. In fact they are both shown to be higher than imposing at 30 Hz. It could be then deduced that imposing at low frequencies could also have some sort of damping effects.

5.4 Flame Tip Response

5.4.1 Harmonic Excitation

Fig. 5.13 shows what is happening to the flame tip at harmonic frequencies. As the excitation starts to reach the flame tip, it begins to react linearly to the imposed frequency. The disturbances shown in the figure shows that the flame tip oscillates at 50, 80 & 120 Hz respective to the excitation frequency applied at the flame base temperature of each.

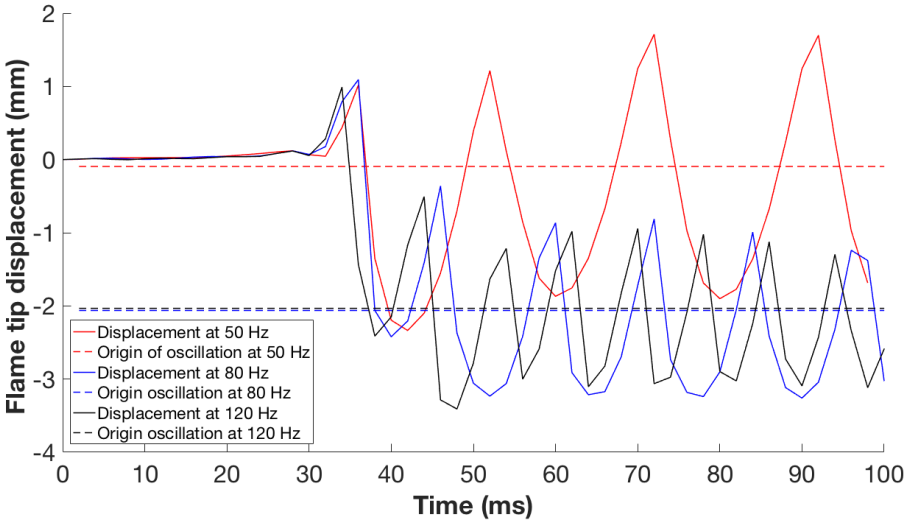

Figure 5.13: Flame tip response excited by 50, 80 & 120 Hz at the flame base temperature.

Moreover, we have noticed that the flame is shortened by introducing higher frequency disturbances. If the flame tip position at steady state is at 0 mm, after imposing the frequencies 80 & 120 Hz the flame tip started to oscillate around -2 mm; i.e. the flame tip is advanced by 2 mm towards the base.

An oscillation or change in the flame tip position implies an oscillation or a change in the flame area. We have already learned that a fluctuation in the flame area could be translated to heat release fluctuation. It could be then deduced that the phenomenon of the flame shortening might have a direct effect on the heat release.

Fig. 5.14 shows that the phenomenon of shortening the flame is just temporary and exclusively depending on the harmonic frequency applied. We can see that after removing the excitation of 120 Hz, the flame tip gets back to its normal position as the case in the steady state.

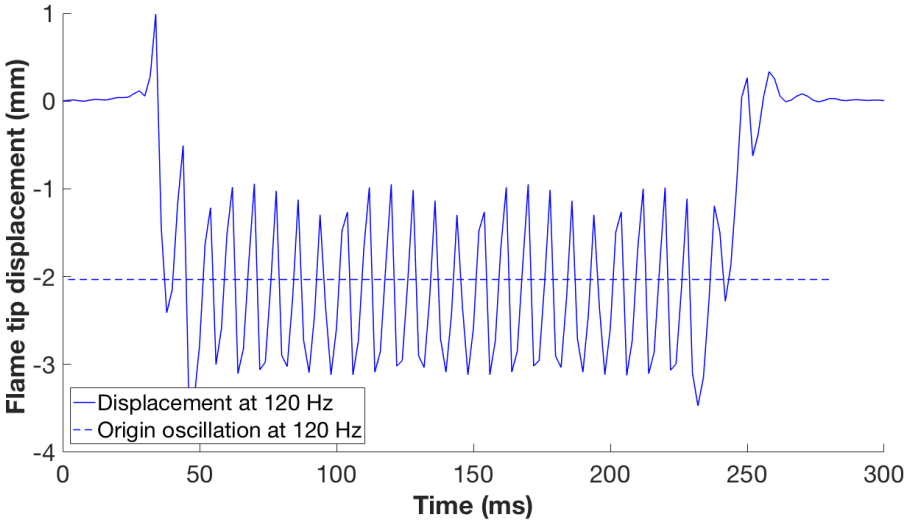

Figure 5.14: Flame tip response after the removal of excitation of 120 Hz.

5.4.2 Impulsive Excitation

Fig. 5.15 shows the response of the flame tip after being exposed to excitation at $0.02s$. We can see that in both excitation methods, it took the flame tip $0.03s$ to start to respond to the excitation. If we divide the inlet velocity component in the flame front direction by the flame front length, we also get the same time. This confirms the theory that the wrinkles are propagating with the convection velocity.

As mentioned in the above subsection, second observation we have seen here is that, even though it is just one impulse given at the flame base, unexpectedly we could see that there is always a secondary oscillation happening at the flame tip. Surprisingly, with temperature excitation this secondary effect is greater in amplitude than the primary one.

If we consider the time shift between the two peaks, we find it to be around 0.012 s which corresponds to a frequency of 83.3 Hz. If you recall from the harmonic frequency test, 80 Hz for this flame was the frequency with the highest growth rate. It is also the frequency with an amplified gain (higher the unity) in our *FTF*. This made us reckon that the secondary wrinkle and the growth rate peak at 80 Hz, which presumably lead to the amplified *FTF* gain, might be somehow correlated.

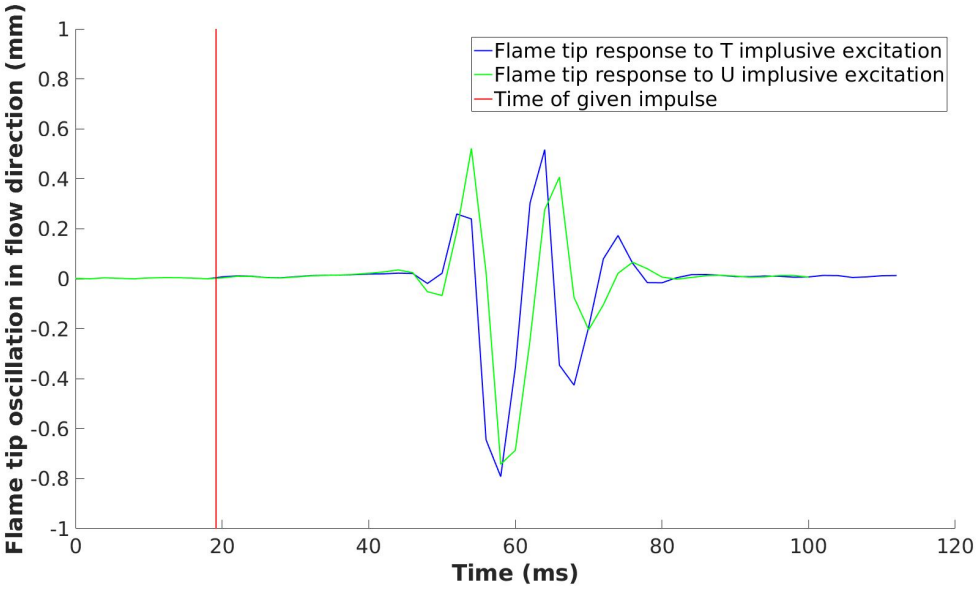

Figure 5.15: Flame tip impulse response.

5.5 Simulation vs Axial Convective Model

In section 2.3.3 we have introduced two models for the prediction of the flame front behavior based on two approaches for velocity modulation. In this section we chose to compare the *axial convective velocity* model to our simulation in terms of flame growth. A *Matlab* tool developed by in the *"Professur für Thermofluiddyanmik"* that solves Eq.(2.41) based on finite differences method was used to model velocity perturbations of an inclined flame with angle $0.28rad$, flame length L = 36 mm and Reynold's number Re = 1300. The inlet velocity was modulated using the two harmonic frequencies 80 Hz and 120 Hz. The same post processing method is applied to the resulting simulations and the following observations were obtained.

Fig. 5.16 and Fig. 5.17 show the flame front behavior for the above mentioned two harmonic frequencies. In these figures, the blue line represents the steady state position of the flame while the red one is the perturbed flame front. The first observation we noticed here is regarding the flame tip. It has been seen that its oscillation is always around the steady state position. In that sense, the model expects that the flame length stays the same and not shortened as we have seen for the respective frequencies in the *OpenFOAM* simulation, Fig. 5.13.

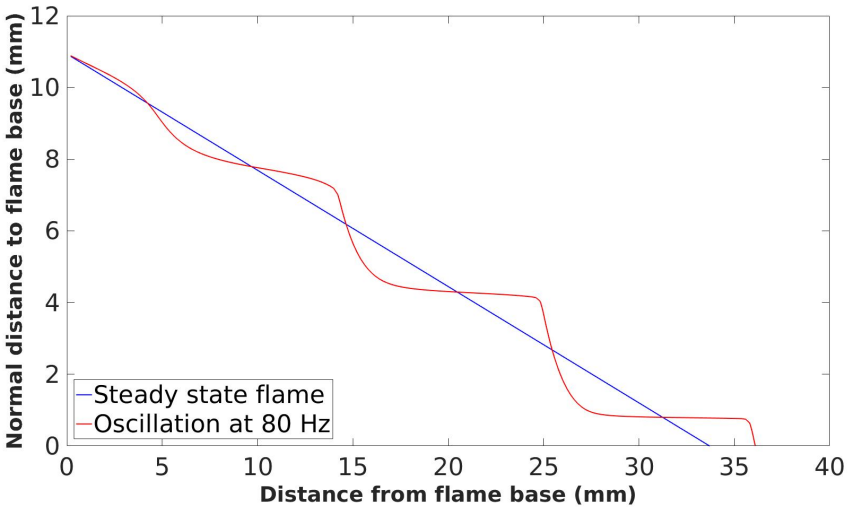

Figure 5.16: Axial convective model flame front behavior at 80 Hz.

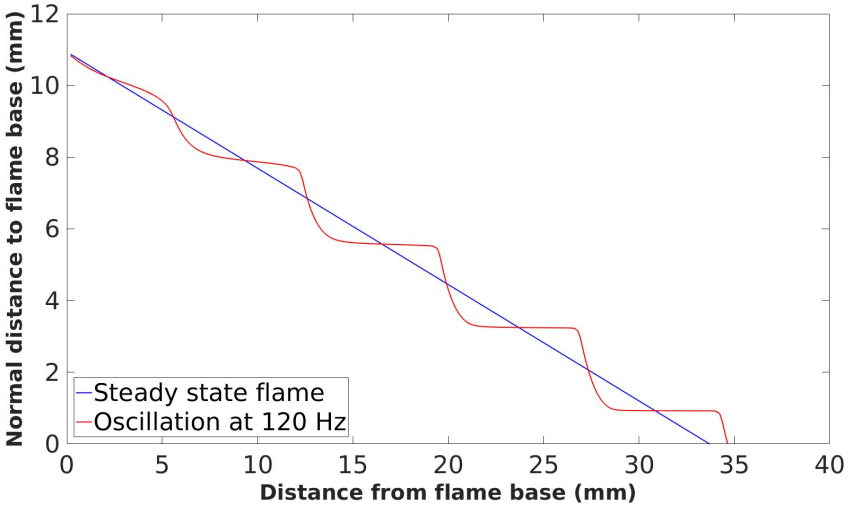

Figure 5.17: Axial convective model flame front behavior at 120 Hz.

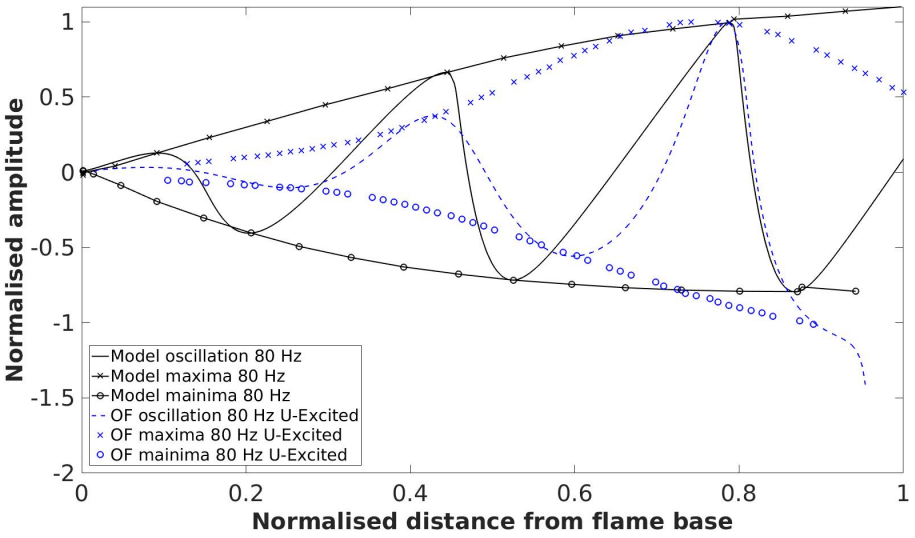

Figure 5.18: Axial convective model vs OF with 80 Hz U-Excitation.

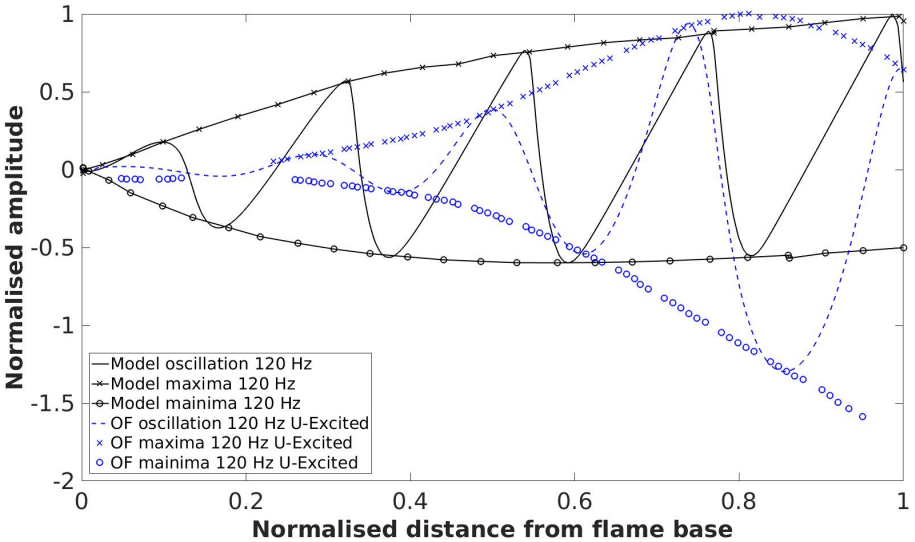

Figure 5.19: Axial convective model vs OF with 120 Hz U-Excitation.

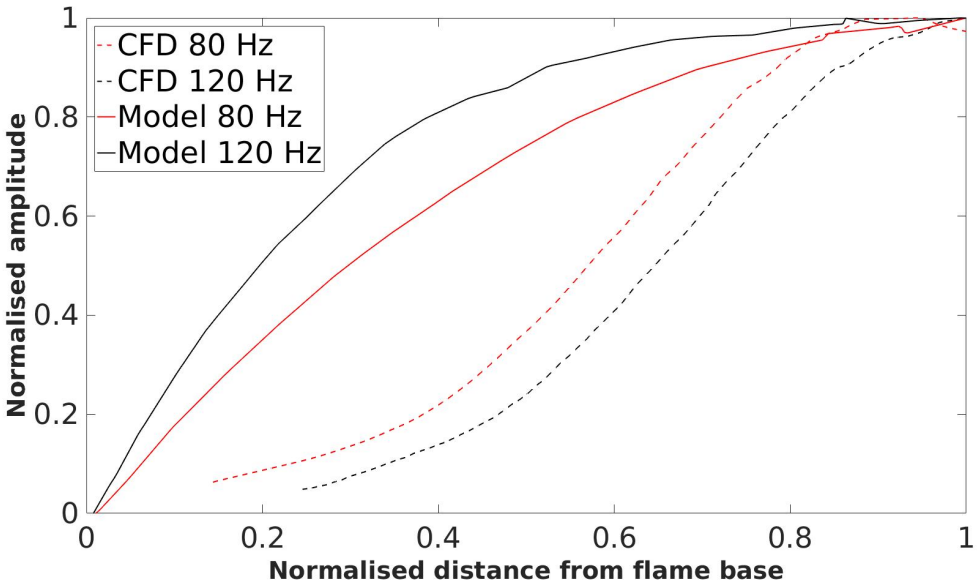

Figure 5.20: Axial convective model vs OF with 120 Hz T-Excitation.

A comparison between the model and *OpenFOAM* simulation can be observed starting from Fig. 5.18. In this context we have considered to compare the model and the simulation with respect to the velocity excitation approach. Figures 5.18 and 5.19 compare them in terms of normal-to-flow oscillations of the flame front. The solid black line is the model oscillation at a certain snapshot while the solid black with crosses $'\times'$ and circles $'\circ'$ are the pattern of the maxima and minima of that oscillation during the whole simulation period. Similarly, oscillation resulting from *OpenFOAM* simulation is represented in the dashed blue line at a certain time snapshot with the blue crosses and circles are its maxima and minima for several snapshots.

On a qualitative analysis, it could be seen that at 80 Hz, represented in Fig. 5.18, the model produces a linear growth with equal amplitudes towards the upstream and downstream sides of the flame front. While the cusps formation resulting from the *OpenFOAM* simulation (blue) produces a higher peak towards the downstream with it being at a normalized distance of around 0.75 from the flame base. Moreover the growth behavior before these peaks appears to be having an exponential pattern, not as linear as the model.

A similar observation has been seen in the cases of 120 Hz but with lower amplitudes, Fig. 5.19. This could be better observed by comparing peak-to-peak growth in Fig. 5.20. Here the solid lines represent the results from the axial convective model, the dashed lines represent the results from *OpenFOAM* with inlet velocity modulation. The harmonic frequency 80 Hz is represented by the red color while the black one represents 120 Hz.

Regardless of the different behavior of the model flame front from that of that of the simulation. It is clear from the model as well as the simulation that imposing at 80 Hz develops a higher growth rate than imposing at 120 Hz. Also the exponential growth rate seen the by the simulation is higher for 80 Hz than for 120 Hz.

6 Summary and Outlook

One of the most problematic issues of lean combustion systems is the occurrence of combustion instability, which is related to coupling between pressure and thermal fluctuations due to unsteady heat release. This kind of instability is a critical issue; as it sometimes leads to damage in the mechanical components of the system. For this reason, it becomes important to be able to predict the thermo-acoustic behavior of the system [3]. In this context, some researchers focus their efforts on the determination of the *Flame Transfer Function* by dealing with the combustion chamber as a black box that is exposed to acoustic perturbations as an input and produces thermal fluctuations as an output. In parallel, some other researchers are more interested in the direct effect of these perturbations on the flame behavior and how it becomes unstable. In this thesis, we have divided our efforts in both directions in order to try to find a link between them.

Summary

We started by introducing the thermo-acoustic system as a network of small elements that one of which is the flame. We then defined the *FTF* and we introduced the effect of the time delay between the input and output perturbations in such a way that one would expect how the gain and phase would look like. In the second part of chapter 2 we have introduced some basic theories regarding the dynamics of laminar premixed flames until we defined the kinematic relation (2.21). From this point we were able to derive the field equation describing the flame position (2.26). This equation gave us a starting point to introduce a general model that describes an inclined flame front displacement in 2D (2.37), which made us able to predict the effect of velocity perturbations by introducing the two models for *uniform velocity perturbations* and *axial convective wave*. In the final section of this chapter, we introduced the flame instability and we focused on the hydrodynamic effects. We introduced the *Landau* model that considers only the hydrodynamic effects, Eq (2.42), then another dispersion relation that additionally takes into account the thermal-diffusive effects, Eq.(2.44).

In chapter 3 we started by deriving an alternative definition for the *FTF* that relates velocity fluctuations to area fluctuations instead of heat release, Eq. (3.5). From this equation we were able to represent an analytical *FTF* based on the flame displacement model approaches explained in the previous chapter. Furthermore, we introduced the transfer function which satisfies the mass balance, Eq. (3.13). In section 3.2 we reviewed the work of *Searby* [28] that included the experimental determination of the Darrieus-Landau instability of V-Flames. It has been seen that the wrinkles amplitude grows exponentially until the point of saturation.

The numerical setup of our case was introduced in chapter 4. *OpenFOAM* was used for our CFD simulation of a lean premixed conical flame. A homogeneous mixture of air and methane

at room temperature is used in the inlet boundary condition. Due to the low speed that resulted in a low Mach number, we have considered an incompressible flow; nevertheless the density could still change due to temperature. The geometry of the combustion chamber has a confinement ratio of 0.44. It was reduced to a 2D mesh for less computational cost and the mesh was refined around the flame front for better computational accuracy. The average inlet velocity is 0.9015 m/s that has a Reynold's number $Re = 1240$. No slip boundary condition was applied to the walls, which were all considered adiabatic except for the chamber radial wall that allowed a heat transfer. Via a boundary condition named $groovyBC$ two functions were implemented that allowed to perturb the flame front. Flame contour data were extracted after simulations and post processing was performed in *Matlab*. This included creating functions to determine the normal-to-flow oscillation of the flame front, extracting its maxima and minima, finding the peak-to-peak amplitude and using least square regression to find the growth rates.

Finally the results were included in chapter 5. We started by comparing the heat release perturbations in response to the impulsive excitation of velocity inlet and temperature base. It was shown that both have a qualitatively quasi-similar behavior. The gain and phase of the *FTF* resulting from a broadband signal were discussed and it was found that the gain has an amplified magnitude of higher than unity at around 80 Hz. The flame front behavior was tested for different harmonic frequencies up to the cutoff frequency (120 Hz) and it was found that when excitation at 80 Hz produced the highest instability (maximum growth rate) of the flame front. Moreover, an impulsive excitation test was made and a secondary wrinkle appeared to be lagging the primary wrinkle with a time delay that corresponds to 83 Hz. We concluded therefore that out of this phenomenon a superposition happened at 80 Hz that lead to the gain amplification of the *FTF*.

Further observations were made for the flame tip response. The flame was found to be shortened when excited at higher frequencies. Also from the impulsive excitation test, the time it took the flame tip to respond to the excitation matched the time calculated by dividing the flame length by the convected velocity along the flame front; which confirmed the theory that wrinkles are convected via the mean inlet velocity component along the flame front. Results from the simulation were compared to results from the axial convective model which had been discussed in chapter 2. It was concluded that while the simulation expects an exponential growth, the model produced a different pattern by predicting a linear growth of the wrinkling amplitude.

Outlook

Some other observations were noted. However, due to the lack of time that lead to insufficient amount of results, it was not possible to come up with conclusions for them. From the results of two simulations of a similar case but with a slit flame instead of conical one, it was found that the flame tip oscillates at an amplitude which is double the value of that for the conical flame case, which indicates the higher instability of slit flames. Same work could be repeated for a slit case in order to determine the Darrieus-Landau instability of slit flames. On the other hand, it was observed that with a confined flame exit, both cases get the same amplitude for

the flame tip oscillations. Therefore, another test could be made regarding the effect of the confinement ratio on the Darrieus-Landau instability.

We know that the area fluctuation is related to heat release fluctuation. Moreover, it was observed that the flame tip fluctuation has a similar pattern to the area fluctuation, which could be related as well to the heat release fluctuation. If one succeeded to develop an equation of motion that describes the flame tip displacement, converting it in the frequency domain could be a good start to develop another analytical *FTF* from a new perspective.

Bibliography

[1] https://chrisbharding.wordpress.com/tag/chapman-and-enskog/.

[2] D. Durox A. Cuquel and T. Schuller. Theoretical and experimental determination of the flame transfer function of confined premixed conical flames. *Italian section of the combustion institute*, 2011.

[3] Antonio Andreini Alessandro Innocenti and Bruno Facchini. Numerical identification of a premixed flame transfer function and stability analysis of a lean burn combustor. *Energy Procedia*, 2015.

[4] Louis Boyer and J. Quinard. On the dynamics of anchored flames. *Combustion and Flame*, 82:51–65, 1990.

[5] Felix Guethe Francois Meili Peter Flohr Bruno Schuermans, Valter Bellucci and Christian Oliver Paschereit. A detailed analysis of thermoacoustic interaction mechanisms in a turbulent premixed flame. *Proceedings of ASME Turbo Expo*, 2004.

[6] C. Clanet and G. Searby. First experimental study of the darrieus-landau instability. *PHYSICAL REVIEW LETTERS*, 80(17):3867–3870, November 1998.

[7] Dr. Andreas Class. *Strömungen mit chemischen Reaktionen*. Karlsruher Intstitut für Technologie.

[8] Paul Clavin and P. L. Garcia-Ybarra. The influence of the temperature dependence of diffusivities on the dynamics of flame fronts. *Journal de Physique Théorique et Appliquée*, 2(2):245–263, 1983.

[9] Alexis Cuquel. *Dynamics and nonlinear thermo-acoustic stability analysis of premixed conical flames*. PhD thesis, Ecole Centrale Paris, 2013.

[10] T. D. Eastop and A.McConkey. *Applied Thermodynamics*. Longman, 1993.

[11] Tarek Echekki and M. G. Mungal. Flame speed measurements at the tip of a slot burner: Effects of flame curvature and hydrodynamic stretch. *Twnety Third Symposium on Combustion / The combustion Institute*, pages 455–461, 1990.

[12] Erwald Freitag. *On the Measurement and Modelling of Flame Transfer Functions at Elevated Pressure*. PhD thesis, Technische Universität München, Lehrstuhl für Thermodynamik, Garching bei München, Germany, December 2008.

[13] Jean-Pierre Hathout. Thermoacoustic instability. In *Fundamentals and Modeling in Combustion*, 1999.

[14] Bhupendra Khandelwal. *Development of Gas Turbines Combustor Preliminary Design Methodologies and Preliminary Assessments of Advanced Low Emission Combustor Concepts*. PhD thesis, Cranfeld University, School of Engineering, July 2012.

[15] Philip Kiameh. *Power Generation Handbook*. McGraw-Hill, 2002.

[16] T. Lieuwen. Modeling premixed combustion-acoustic wave interactions: A review. *JOURNAL OF PROPULSION AND POWER*, 19, 2003.

[17] D. Sipp M. Blanchard, T. Schuller and P. J. Schmid. Response analysis of a laminar premixed m-flame to flow perturbations using a linearized compressible navier-stokes solver. *Physics of Fluids*, 27, 2015.

[18] Moshe Matalon. Intrinsic flame instabilities in premixed and nonpremixed combustion. *Annual Review of Fluid Mechanics*, 39:163–191, 2007.

[19] L. P.M. De Goey J.H.M. ten Thije Boonkkamp R.M.M. Mattheij M.L. Bondar, K.R.A.M. Schreel. Flame dynamics using the level set equation.

[20] Norbert Peters. Combustion theory. CEFRC Summer School, Pricenton, 2010.

[21] Prof. Dr.-Ing. Heinz Pitsch. Laminar premixed flames: Kinematics and burning velocity. Lecture 4, CEFRC Combustion Summer School, 2014.

[22] Wolfgang Polifke. Combustion instabilities. Lehrstuhl für Thermodynamik, Technische Universität München, Germany, 2004.

[23] E. A Gopalakrishnan S. Bomberg R. I. Sujith W. Polifke S. Jaensch, M. Merk. Hybrid cfd/low-order modeling of nonlinear thermoacoustic oscillations. *Combustion Symposium number 36*, 2016.

[24] T. Sattelmayer and W. Polifke. A novel method for the computation of the linear stability of combustors. *Combustion Science and Technology*, 2003.

[25] Bruno Schuermans. *Modeling and Control of Thermoacoustic Instabilities*. PhD thesis, École Polytechnique Fédérale de Lausanne, 2003.

[26] Geoff Searby. Experimental studies of instabilities of laminar premixed flames. Technical report, Institut de Recherche sur les Phénomènes Hors Équilibre, CNRS / Université de Provence, 49 rue Frédéric Joliot-Curie, 13384 MARSEILLES Cedex 13, France, 2004.

[27] D. Durox T. Schuller and S. Candel. A unified model for the prediction of laminar flame transfer functions: comparisons between conical and v-flame dynamics. *Combustion and Flame*, 134:21–34, 2003.

[28] JEAN-MARIE TRUFFAUT and GEOFF SEARBY. Experimental study of the darrieus-landau instability on an inverted-'v' flame, and measurement of the markstein number. *Combustion Science and Technology*, 149(1-6):35–52, 1999.